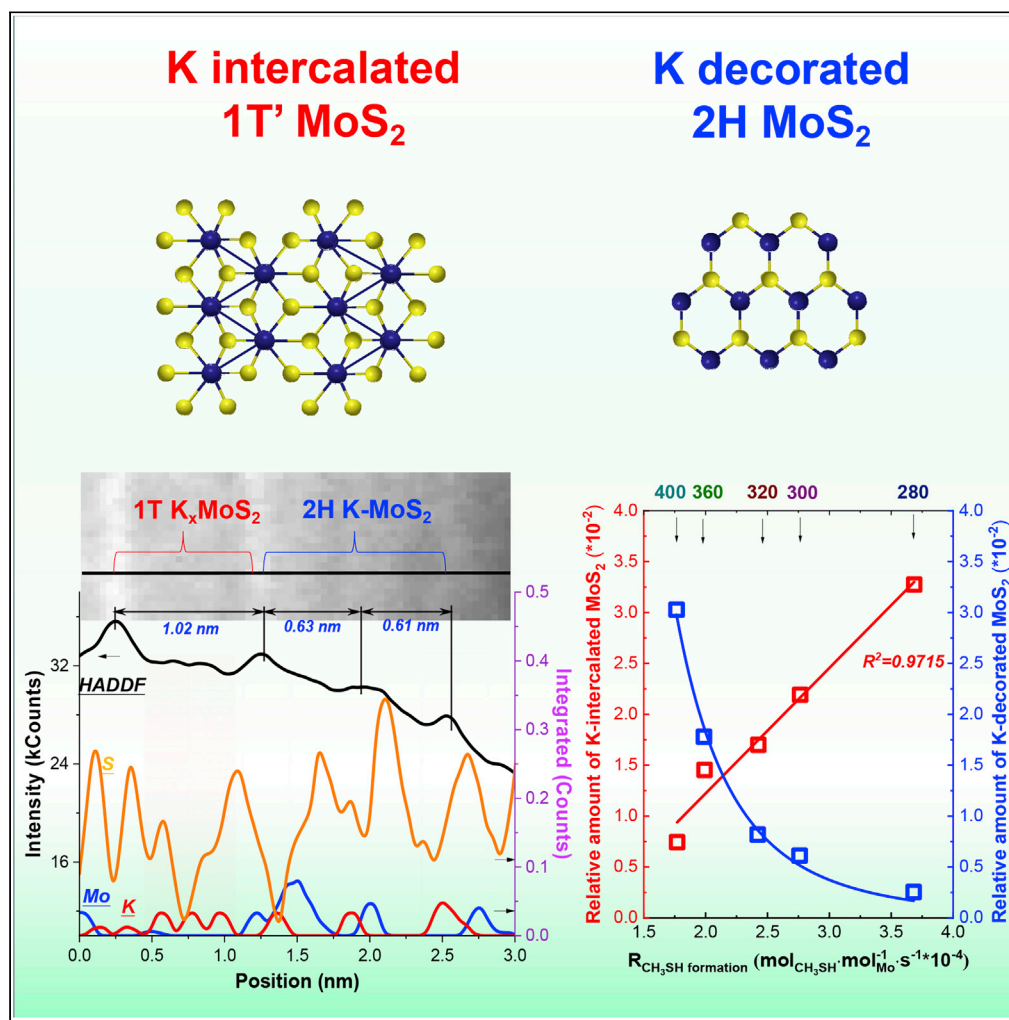## Article

The nature of K-induced 2H and 1T'-MoS$_2$ species and their phase transition behavior for the synthesis of methanethiol (CH$_3$SH)

Zhizhi Xu, Jian Fang, Jichang Lu, Dedong He, Sufang He, Yongming Luo

lujichangc7@kust.edu.cn (J.L.)
environcatalysis@kust.edu.cn (Y.L.)

Highlights

Converting sulfur-containing pollutants with syngas (CO/H$_2$/H$_2$S) is promising

Thermally induced K-position-dependent phase transformation of MoS$_2$ was reported

The precise position of K over MoS$_2$ was proved at the atomic level

Relationship between MoS$_2$ phases and property for synthesizing CH$_3$SH was established

Article

The nature of K-induced 2H and 1T'-MoS$_2$ species and their phase transition behavior for the synthesis of methanethiol (CH$_3$SH)

Zhizhi Xu,[1,3,4,5] Jian Fang,[2,4,5] Jichang Lu,[1,2,4,5,*] Dedong He,[1,4,5] Sufang He,[2,4,5] and Yongming Luo[1,2,4,5,6,*]

SUMMARY

The one-step reaction approach from syngas with hydrogen sulfide (CO/H$_2$/H$_2$S) over potassium (K) promoted Molybdenum disulfide (MoS$_2$) materials can provide alternatives for the synthesis of methanethiol (CH$_3$SH). However, the direct confirmation and determination of the real active nature of K-induced 2H and 1T'-MoS$_2$ for this reaction and the corresponding phase transformation behavior and origin of K-induced 2H-MoS$_2$ from/to 1T'-MoS$_2$ remains unclear. Herein, we proved at the atomic level the precise position of K over 1T'-MoS$_2$ and 2H-MoS$_2$ species using the technique of HAADF-STEM. A relationship between K-induced 1T' and 2H-MoS$_2$ phases and the catalytic property to synthesize CH$_3$SH was established, and K-intercalated 1T'-MoS$_2$ phase was confirmed to have excellent catalytic performances. Moreover, the behavior, origin, and influencing factors of phase transformation of 2H-MoS$_2$ from/to 1T'-MoS$_2$ in the existence of K were well proved.

INTRODUCTION

Methanethiol (CH$_3$SH) is an important sulfur-containing intermediate for producing pharmaceuticals, pesticides, and especially methionine, an essential amino acid for humans and other animals, which cannot be synthesized in the human body and should be obtained outside the body (Lu et al., 2020a, 2020b). The traditional method for the synthesis of CH$_3$SH focuses on the catalytic reaction of hydrogen sulfide (H$_2$S) with methanol (CH$_3$OH) (Gutiérrez et al., 2011a, 2011c). However, CH$_3$OH should be produced from syngas (CO/H$_2$), and this multi-step reaction gives rise to the enhanced consumption of resource and energy. Considering that CO/H$_2$ and H$_2$S are simultaneously produced from coal gasification, and H$_2$S can be enriched using low-temperature methanol washing technology, the one-step reaction approach from CO/H$_2$/H$_2$S can provide alternatives for the synthesis of CH$_3$SH (Gutiérrez et al., 2011a; Lu et al., 2018, 2020a, 2020b).

High-performance catalysts with high conversion and high selectivity are the key factor to realize the synthesis of CH$_3$SH. Potassium (K) promoted Molybdenum disulfide (MoS$_2$)-based materials are the most widely used catalysts for this reaction owing to the excellent ability for the adsorption and activation of H$_2$S, CO, H$_2$ molecules (Gutiérrez et al., 2011a; Lu et al., 2020a). However, in fact, the obtained conversion of CO and the selectivity of CH$_3$SH over K promoted MoS$_2$-based materials could not reach the requirement of ideal catalysts (Gutiérrez et al., 2011b; c). The main cause for the low catalytic performances is the insufficient knowledge of the real active phases over K-promoted MoS$_2$-based catalysts, limiting the rational design and synthesis of high-performance catalysts (Chen et al., 2008; Cordova et al., 2015; Yu et al., 2020). There are several controversial views on K promoted MoS$_2$ active phases within the system of H$_2$S/CO/H$_2$ (Cordova et al., 2015; Gutiérrez et al., 2011a; Yu et al., 2020). The "K-Mo-S" phase mixed with a different valence of Mo^{n+} (n = 4, 5, 6) was first found to be closely related to the catalytic activity, where increasing the concentration and chemical environment of the Mo^{5+} improved the selectivity of CH$_3$SH, while the detailed microstructure of "K-Mo-S" phase was unclear (Chen et al., 2008; Yang et al., 2000). Lercher et al. proposed a detailed microstructure of K decorated MoS$_2$ species with the decoration of K on the undercoordinated Mo edge, which promoted the hydrogenation of intermediates, COS and CS$_2$, into CH$_3$SH (Gutiérrez et al., 2011a, 2011c). Nevertheless, a lacking of direct and solid evidence on the determination of this K-decorated MoS$_2$ species discounts the attribution of the active phase for the synthesis of CH$_3$SH. Subsequently, a new active species of intercalated K$_x$MoS$_2$ proposed by Lamonier

[1]Faculty of Chemical Engineering, Kunming University of Science and Technology, Kunming 650500, P. R. China

[2]Faculty of Environmental Science and Engineering, Kunming University of Science and Technology, Kunming 650050, P.R. China

[3]Yunnan Research Academy of Eco-environmental Sciences, Kunming 650093, P. R. China

[4]The Higher Educational Key Laboratory for Odorous Volatile Organic Compounds Pollutants Control of Yunnan Province, Kunming 650500, P. R. China

[5]The Innovation Team for Volatile Organic Compounds Pollutants Control and Resource Utilization of Yunnan Province, Kunming 650500, P. R. China

[6]Lead contact

*Correspondence:
lujichangc7@kust.edu.cn
(J.L.),
environcatalysis@kust.edu.cn
(Y.L.)

https://doi.org/10.1016/j.isci.2022.104999

et al. was detected by X-ray photoelectron spectroscopy (XPS), and was deemed to have high catalytic performance for the synthesis of CH_3SH (Cordova et al., 2015, 2017). This intercalated species with trigonal (1T) structure is considered to have distinct difference in the structural properties with K decorated MoS_2 species with hexagonal (2H) structure (Lu et al., 2020b). Nevertheless, the direct comparison of the catalytic performance between intercalated K_xMoS_2 and K-decorated MoS_2 species under identical conditions cannot be found in this field (Cordova et al., 2015; Gutiérrez et al., 2011a; Lu et al., 2020b; Yu et al., 2020).

In some cases, the question raises that the phase of intercalated K_xMoS_2 species was reported to be not unstable and was sensitive to the pressure (Gutiérrez et al., 2011a; Liu et al., 2018; Tang and Jiang, 2015; Yu et al., 2020). In the study of Lamonier et al., the condition in the reaction process was usually high pressure, while the condition for preparing the sample and detecting intercalated K_xMoS_2 by XPS was under the atmosphere pressure (Cordova et al., 2015, 2017). The obvious inconsistency between these conditions drives the researcher to consider the effect of high pressure on the intercalated K_xMoS_2 phase and its catalytic performance. Hensen et al. performed the catalytic test of the 1T-MoS_2 phase under the high pressure of 10 bar and the high temperature of 350°C, and also the subsequent characterization of XPS under the same conditions (Yu et al., 2020). Their results showed that there was no correlation between the productivity of CH_3SH and the number of 1T-MoS_2 phase under harsh conditions. This result contradicts severely the results of Lamonier et al. (Cordova et al., 2015). We assume if all the reactions and characterization undergo relative mild conditions, like atmosphere pressure and low temperature, and the 1T-MoS_2 phase might be survived, whether the 1T-MoS_2 phase can be acted as the effective active center or not remains to be investigated. In general, it is difficult to reach a consensus from current literature about what is the real active phase for the synthesis of CH_3SH, K-induced 2H or 1T MoS_2 (Cordova et al., 2015; Gutiérrez et al., 2011a; Lu et al., 2020b; Yu et al., 2020). These controversies on active phase of K-induced 2H and 1T-MoS_2 might be originated from the following causes.

On the one hand, as K-induced 1T-MoS_2 phase is reported to be unstable under some definitive conditions, the effect of possible differences between the reaction and characterization conditions (temperature, pressure, time) on the stability property of K-induced 1T-MoS_2 phase are presented, which is the main external cause. On the other hand, the dominating internal cause is the lacking of in-depth cognition of the inherent microstructure of K-induced 2H or 1T MoS_2 in the presence of K, especially the position of K over MoS_2 and the dynamic evolution of K during the thermal treatment, as well as a systematic study on their influence on the catalytic performance for the synthesis of CH_3SH. Unusually, alkali metals, such as K, have been shown to be an important promoter in many fields (Lee et al., 1994; Liu et al., 2016). As reported, K could modify the surface coordination environment via the creation of –O, –OH, and –SH linkages and stabilize the microstructures of active phases (Bai and Li, 2014; Hao et al., 2019; Yang et al., 2014). Specifically, the position of K over active phases plays an important role in the catalytic performance. For instance, in the NH_3-SCR reaction, the covering of K on the surface of α-MnO_2 deceased the NO_x conversion from 50.6% to 23.2%, while the incorporation of K into the lattice of α-MnO_2 largely increased the NO_x conversion from 50.6% to 100% (Hao et al., 2019). Moreover, there has been very little research into the phase transformation behavior, origin, and influencing factors of 2H-MoS_2 from/to 1T(T')-MoS_2 under the presence of K, which further hinders the depth insight into the active site and the reaction mechanism for the synthesis of CH_3SH.

In this work, the different amounts of K-induced 2H/1T'-MoS_2 phases (K-intercalated 1T'-MoS_2 and K-decorated 2H-MoS_2) were controllably synthesized by using a facile K-induced thermal driven tuning method. We gave an insight into the position and role of K over MoS_2, and also an understanding of the phase transition origin, factors, and behaviors between K-induced 2H and 1T'-MoS_2 phases. The specific location and atomic distribution of K on 1T' and 2H-MoS_2 phases were directly demonstrated at the atomic level by aberration-corrected scanning transmission electron microscopy (STEM) with high-angle annular dark-field (HAADF) line scan modes. Furthermore, the characterization conditions were matched with that during reaction processes, and the relationships between individual phases (K-decorated 2H-MoS_2 or K-intercalated 1T'-MoS_2) and the catalytic performance for synthesizing CH_3SH were established under the mild and identical conditions.

RESULTS AND DISCUSSION
Synthesis and characterization of K-intercalated 1T'-MoS_2 and K-decorated 2H-MoS_2 phases
The phase transformation between 1T'-MoS_2 and 2H-MoS_2 under the assistance of K was achieved by vulcanizing the microspherical silica (MS) based monoclinic K_2MoO_4 samples in the
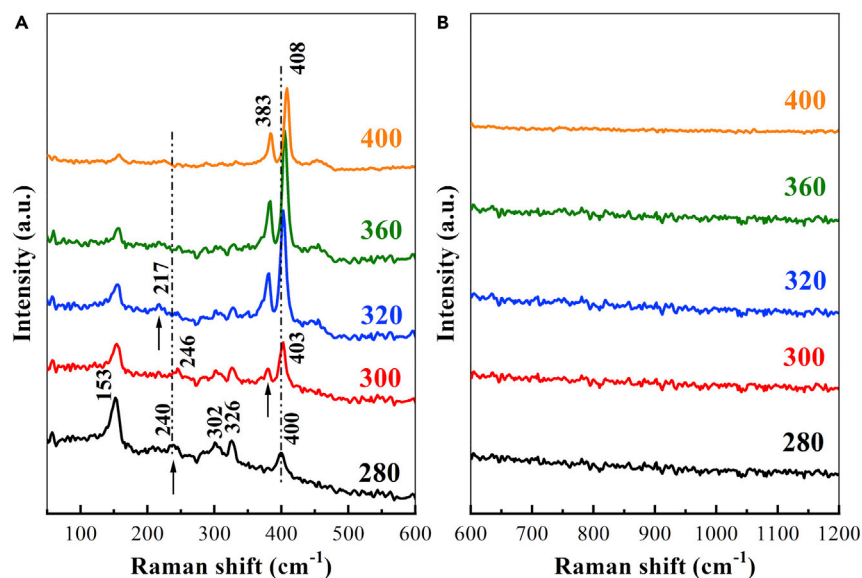
Figure 1. Raman spectra of K-Mo/MS catalysts

Raman spectra in the range of 50-600 cm^{-1} (A) and in the range of 600-1200 cm^{-1} (B) of K-Mo/MS catalysts sulphided at 280, 300, 320, 360, 400°C, respectively.

continuous flowing of H_2S/H_2 mixtures with tuned thermal annealing temperatures (280, 300, 320, 360, 400°C). This method allows the facile production of K-intercalated 1T'-MoS$_2$ and K-decorated 2H-MoS$_2$ species.

Raman spectroscopy was used to investigate the evolution of structural characteristics and compositions during the phase transformation. First, the different atomic arrangement and symmetry modes between Mo and S suggest the presence of different chemical environments of MoS$_2$, which would give rise to the large differentiation in Raman signals. When the K-Mo sample was sulphided at 280°C, four Raman peaks at 153 cm^{-1} (A$_2$ mode), 302 cm^{-1} (A$_g$ mode), 326 cm^{-1} (A$_1$ mode), and 400 cm^{-1} (A$_{1g}$ mode) are observed (Figure 1A), which proves the presence of the intercalated 1T' MoS$_2$ structure (Liu et al., 2018). One special peak at around 240 cm^{-1} is attributed to the out-of-plane K-S Raman mode in the intercalated MoS$_2$ species (Tan et al., 2017). These results confirm that K-intercalated 1T' MoS$_2$ species are formed and no other additional species is presented when sulphided at 280°C (as also confirmed by the absence of distinct Raman peaks in the range of 600-1200 cm^{-1} (Figure 1B)). With the vulcanization temperature increasing to 300°C, the well-known 2H MoS$_2$ phase emerges (the new peaks at about 383 cm^{-1}, 403 cm^{-1}, and the weak signal at 453 cm^{-1}, assigned to the in-plane E$^1_{2g}$, out-of-plane A$_{1g}$, and second order scattering, respectively). As reported in the literature, the A$_{1g}$ mode of the 1T' MoS$_2$ species at 400 cm^{-1} is similar to that of 2H MoS$_2$ species at 403 cm^{-1} (as well as 408 cm^{-1} for the sample sulphided at 400°C), while the Raman peak of 383 cm^{-1} is unique to a typical 2H MoS$_2$ phase (Tan et al., 2017). The decreased intensities of Raman peaks of 1T' MoS$_2$ structure and the appearance of Raman peaks of 2H MoS$_2$ phase indicate the occurrence of phase transformation of MoS$_2$ as the thermal vulcanization temperature varied. Notably, a slight change in the position of the Raman peak (from 240 cm^{-1} to 246 cm^{-1}) is observed. As Raman spectroscopy is a useful tool to characterize the vibration of metal-oxygen bonds and their surrounding chemical environment, this change corresponds to the possible alteration in the chemical environment of K-S from 1T' MoS$_2$ species to 2H-MoS$_2$ owing to the change in the distance of K-S bond (Andersen et al., 2011). The K species in the K-intercalated 1T' MoS$_2$ is believed to be located at the gaps between MoS$_2$ layers (confirmed in the STEM characterization). As the phase transition occurred, the intercalated K would be pushed out from the MoS$_2$ layers and might be decorated at the edge of MoS$_2$ via K-S linkages (246 cm^{-1}, Figure 1A), resulting in the formation of the K-decorated MoS$_2$ species. As the vulcanization temperature further increased from 320 to 400°C, the strongest peak at 153 cm^{-1} related to the 1T' MoS$_2$ structure gradually weakens, indicating that K-intercalated 1T' MoS$_2$ is gradually converted into the K-decorated 2H MoS$_2$ species, induced by K position-dependent phase transformation.
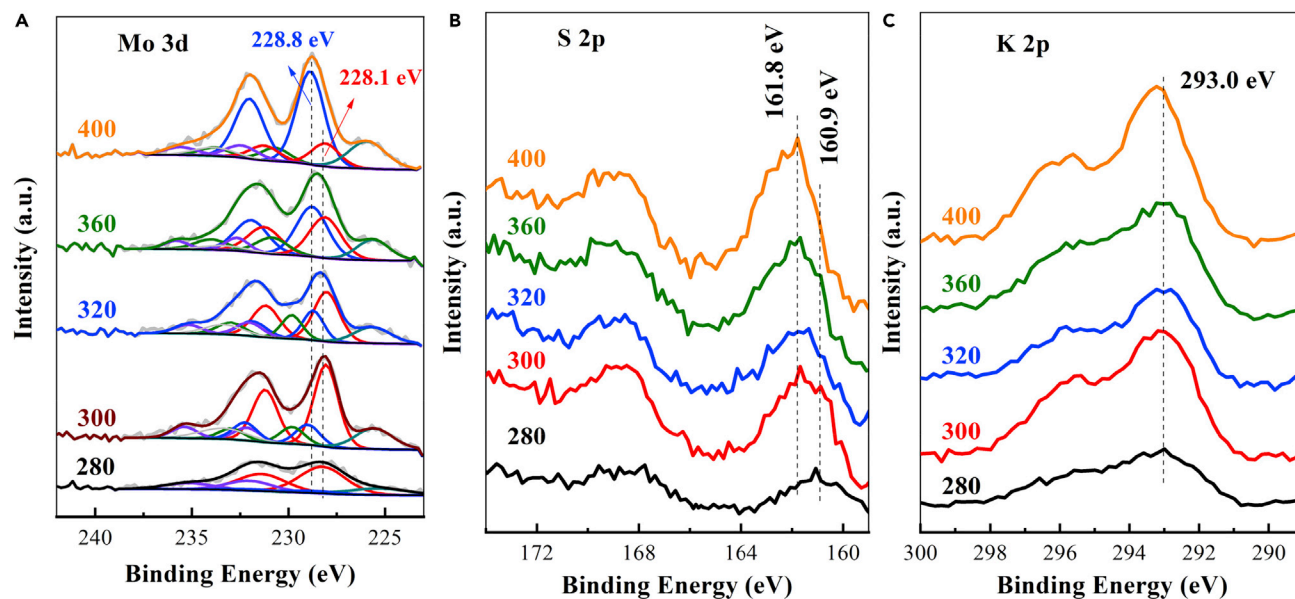
Figure 2. XPS spectra of K-Mo/MS catalysts
XPS spectra of Mo 3d (A), S 2p (B), and K 1 s (C) of K-Mo/MS catalysts sulphided at 280, 300, 320, 360, and 400°C, respectively.

In agreement with the Raman result, X-ray photoelectron spectroscopy (XPS) spectra in Figure 2 and Figure S1 also demonstrate the properties of K-intercalated 1T' MoS_2 and K-decorated 2H MoS_2 species as well as their phase transformation behavior. As known, a typical 2H MoS_2 phase has a binding energy of around 229.0 eV (Eda et al., 2011; Wang et al., 2013; Zhang et al., 2016). As K is a typical electronic donor, the decoration of K on the edge of MoS_2 would induce the slight donation of a 4 s valence electron of K into empty d orbits of Mo, which could increase the electron density of Mo and thus slightly decrease the binding energy to 228.8 eV (Lu et al., 2020b). This binding energy can be attributed to K-decorated 2H MoS_2 species, which is also identified by S $2p_{3/2}$ XPS peaks at around 161.8 eV as well as the K $2p_{3/2}$ XPS peaks at 293.0 eV (Figures 2A, 2B, and 2C). Moreover, a new peak at 228.1 eV appears, and the binding energy of Mo 3d XPS shifts toward lower value compared to that of K-decorated 2H MoS_2 species. This peak should be assigned to the presence of K-intercalated 1T' MoS_2. With the transformation of the phase structure from hexagonal 2H MoS_2 to octahedral 1T' MoS_2, the electron transfer ability from K 4 s to Mo 3d is enhanced and the intercalated K would donate large amount of electrons to MoS_2 leading to reduced binding energy (Lu et al., 2020b; Zhang et al., 2016), which is also proved by S 2p XPS peaks at around 161.0 eV as well as K $2p_{3/2}$ XPS peaks at 293.0 eV (Figures 2A, 2B, and 2C). As the vulcanization temperature increases to 400°C, the amount of K-intercalated 1T' MoS_2 gradually decreases, and the amount of K-decorated 2H MoS_2 increases, indicating the occurrence of thermally induced K-position-dependent phase transformation from K-intercalated 1T' MoS_2 to K-decorated 2H MoS_2.

As the coordination geometries of Mo and S atoms are different in 2H and 1T' MoS_2, differentiating the K-intercalated 1T' MoS_2 and K-decorated 2H MoS_2 at the atomic scale is possible. Thus, the corresponding microstructures of the two phases were characterized by an atomically resolved HAADF-STEM imaging technique. As a typical layered material, MoS_2 consists of molecular layers stacked by weak van der Waals interactions. The weak interlayer interaction causes the guests to be intercalated into gaps between layers to expand the interlayer spacing. Thus, interlayer spacing can be first considered as a characteristic sign to identify the different phase structures. STEM-HAADF image of the sample sulphided at 320°C as a representative (Figure 3A) shows the presence of a clear lattice fringe with the interlayer spacing of 0.62 nm, which corresponds to the (002) basal plane of typically MoS_2 species (between 0.61 and 0.63 nm) (Kong et al., 2013; Liu et al., 2015a; Zhang et al., 2015). In the other regions in the same sample (Figure 3B), the fringes with an expanded interlayer distance of about 0.68 nm or 0.89 nm wider are observed, revealing the existence of intercalated MoS_2 species. The high-resolution STEM-HAADF image in Figure 3C has clearly visualized that Mo and S atoms are arranged with an interlaced net, where an Mo atom is linked with four S atoms, and two long-bond or short-bond S atoms are located on the same side, in agreement
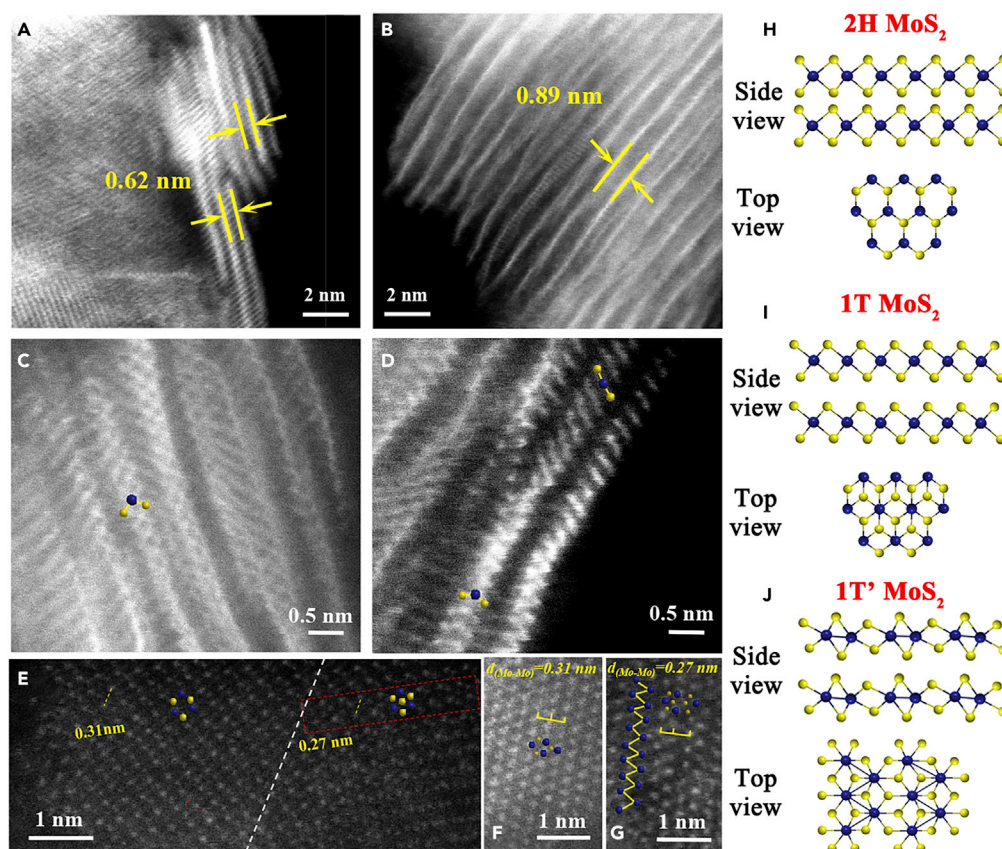
Figure 3. HADDF-STEM images of K-Mo/MS catalysts
The representative HADDF-STEM images of K-Mo/MS catalyst sulphided at 320°C, where (A) and (B) are the images from side view, (C) and (D) are the corresponding enlarged images; (E), (F) and (G) are the images from top view; the structures schematic of 2H-MoS₂ (H), 1T-MoS₂ (I) and 1T'-MoS₂ (J).

with the theoretical unit cells of 2H MoS₂ displayed in Figure 3H. Also, from high-resolution STEM-HAADF imaging in Figure 3D, the arrangement of Mo with the S atom in a straight chain is atomically observed, where the Mo atom is linked with two long-bond or short-bond S atoms in the diagonal position, consistent with the unit cells of 1T and 1T' MoS₂ as shown in Figure 3I. Except for the observation of 2H and 1T(1T') MoS₂ from the side view, the direct atomic visualization of two microstructures from the top view can be achieved. As shown in model unit cells in Figure 3H (top view), the hexagonal Mo lattice in 2H MoS₂ is sandwiched with hexagonally packed S, where the coordination of Mo with S is trigonal prismatic, and the stacking sequence is AbA BaB (the lower and capital case letters denote Mo and S atoms, respectively). This microstructure of 2H MoS₂ with a hexagonal lattice is distinctly observed by STEM-HAADF imaging of single-layer 2H MoS₂ in Figure 3E, where the signal intensity of Mo in the hexagonal lattice is stronger than that of the S atom owing to the higher atomic number (Z). The measured nearest Mo-Mo distance of 0.31 nm in the hexagonal lattice is also a signature of 2H MoS₂ (Liu et al., 2015b; Voiry et al., 2013b). With the gliding of one S planes into the hexagonal lattice center of 2H MoS₂, the phase transition from 2H to 1T(1T') MoS₂ occurs, where the coordination of Mo with S becomes octahedral and the stacking sequence becomes AbC, as seen from model unit cells in Figure 3I (top view). The atomically resolved STEM-HAADF image (Figure 3E) clearly shows that S atoms with weak signal intensities are located at the center of the distorted trigonal lattice with a marked Mo-Mo distance of 0.27 nm (Liu et al., 2015b; Tan et al., 2017; Voiry et al., 2013b), proving the presence of the 1T MoS₂ phase with a distorted structure, i.e., 1T' MoS₂. The 1T' MoS₂ phase possesses a √3x1 superlattice structure as visualized in Figure 3G and this species is deemed to originate from the distortion of the metastable 1T MoS₂ phase (Goki Eda et al., 2012). Compared to 2H MoS₂ (Figure 3F), the observed zigzag chain-like patterns shown in Figure 3G are another signature of the 1T' MoS₂ phase. Based on the above HAADF-STEM results, we demonstrate at the atomic level the presence of 2H and 1T' MoS₂ phases in the supported K-Mo/MS samples.
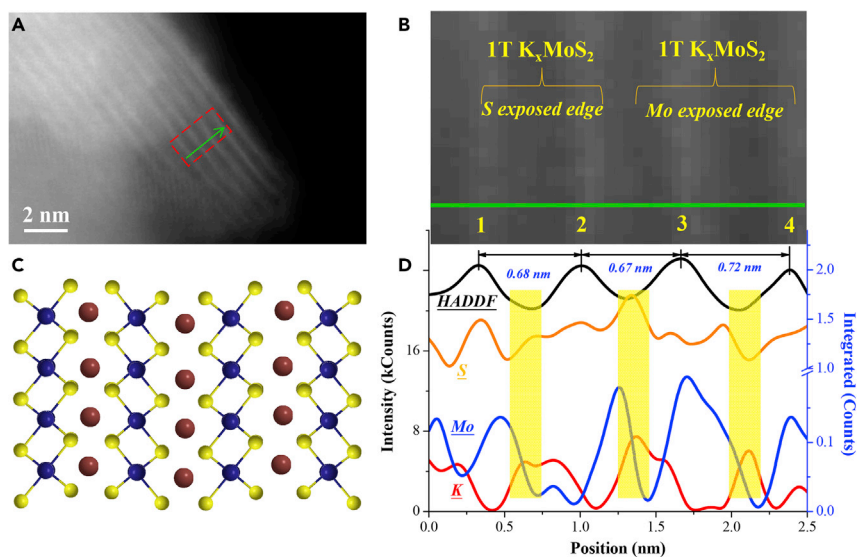
Figure 4. HADDF-STEM images of 1T′ K$_x$MoS$_2$

K-Mo/MS catalyst sulphided at 320°C showing the selected HADDF-STEM image (A), the enlarged image (B) in (A), the cell schematic (C), and the line scanning result (D) of K-intercalated 1T′-MoS$_2$ (1T′ K$_x$MoS$_2$).

Confirmation of the position and atomic distribution of K over MoS$_2$-like phases

Despite the microstructures of 2H and 1T′ MoS$_2$ phases were evidenced, the direct observation of the location of K in the MoS$_2$ phases is difficult (Liu et al., 2018; Wang et al., 2014a), and it is also a challenge to precisely determine the position of K over different catalysts in the fields of heterogeneous catalysis and materials science, owing to the fact that potassium is a light metal and has the very weak scattered electron intensity in the STEM imaging (Cheng et al., 2014; Liu et al., 2018; Wang et al., 2014a). To confirm the occupancy of K in MoS$_2$, we have further performed the Z-contrast in HAADF-STEM images with line-map scanning mode at the atomic level.

The corresponding line scanning results of the selected HADDF-STEM image of K-Mo/MS catalyst sulphided at 320°C were obtained by processing the map scanning data using the software of GMS, as shown in Figure 4 and Figure 5. Figure 4D exhibits the intensity profile recorded along the green line with a nanoscale width as signed in Figure 4A. As shown in the megascopic Figure 4B followed with the profile of Figure 4D, the black line recorded with the HAADF signal intensity shows four mountain-shaped peaks (marked as 1, 2, 3, and 4 from left to right), matching well with the bright fringe of MoS$_2$ in Figure 4B. The measured expanded interlayer spacing of 0.68-0.72 nm indicates the presence of the intercalated MoS$_2$ phase by one or two K atom (Dai et al., 2015; Hu et al., 2014; Ling et al., 2017). In the region from 1 to 2 peaks, the strong peaks of elemental S (yellow line) are directly located below the top of the HAADF peaks and the signal of elemental Mo (blue line) is very weak, revealing that the intercalated MoS$_2$ phase exhibits the S-exposed edges. Notably, in this case, the strong peak of elemental K (red line) is directly located below the valley of HAADF peaks (yellow region), suggesting that K atoms are located between the gap of two MoS$_2$ stripes, which demonstrates the formation of the K intercalated 1T′ MoS$_2$ phase with S exposed edges. In the region from 3 to 4 peaks, the location of the signal peak of elemental Mo below the top of the HAADF peaks proves that the intercalated MoS$_2$ phase displays the Mo-exposed edges. For this region, the strong peak of K is properly located below the valley of HAADF peaks (K has a distance of 0.28 nm with Mo atom), demonstrating the intercalation of K into the gap of the 1T′ MoS$_2$ phase with Mo-exposed edges.

Meanwhile, in other selected HAADF-STEM region, as shown in Figure 5, three small K peaks are actually located between two MoS$_2$ fringes (yellow region), and the interlayer spacing is expanded to 1.02 nm, confirming the intercalation of K into 1T′ MoS$_2$ phase by three K atoms and forming K-intercalated MoS$_2$ species. Some researches also reported that a substantial increase in the interplanar spacing with 0.3-0.5 nm could be observed for intercalated MoS$_2$/WS$_2$ phases during the preparation of superconducting layered
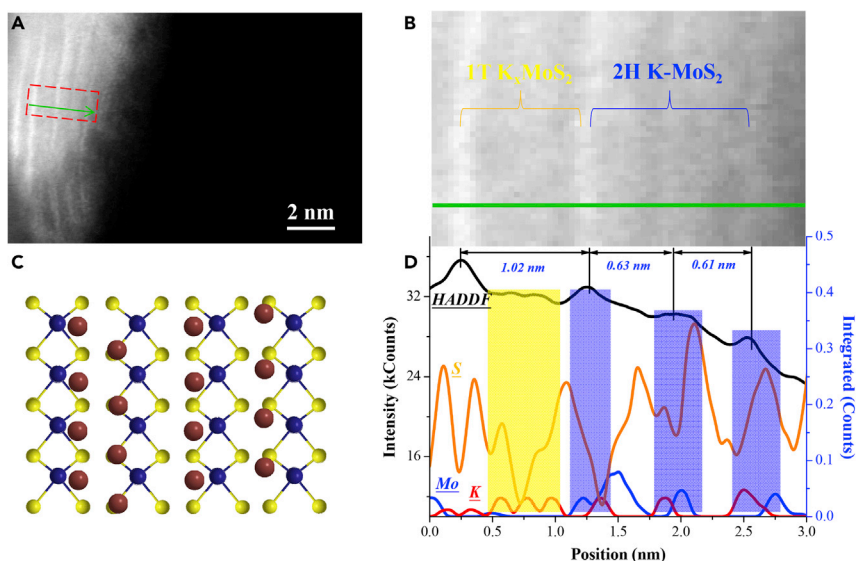
Figure 5. HADDF-STEM images of 2H K-MoS₂
K-Mo/MS catalyst sulphided at 320°C showing the selected HADDF-STEM image (A), the enlarged image (B) in (A), the cell schematic (C), and the line scanning result (D) of K-decorated 2H-MoS₂ (2H K-MoS₂) and K-intercalated 1T'-MoS₂ (1T' K$_x$MoS₂).

materials using the liquid method or vapor transport technique (Zak et al., 2002; Zhang et al., 2016). In addition, the occupancy of K over the 2H MoS₂ phase can also be evidenced by the line scan mode of the HAADF-STEM image. As shown in Figures 5B and 5D, there are three MoS₂ fringes (blue region) with the interlayer spacing of 0.61-0.63 nm, suggesting the existence of 2H MoS₂ species. Note that the signal peak of the K atom is found to be located below the top of the HAADF peaks and has a closely linkage with that of the Mo atom (0.13 nm). Meanwhile, no additional signal peaks of K element are found to be located below the valley of the HAADF peaks, i.e., no K atom is located between the gap of MoS₂ fringe layers. All the phenomena clearly demonstrate that the K atom is decorated at the Mo edge in the 2H MoS₂ phase. According to the above line scan mode of the HAADF-STEM image, we have visualized at the atomic level that K atoms in the 1T' MoS₂ are intercalated into the gap of fringe MoS₂ layers, then forming a K-intercalated 1T' MoS₂ phase, and K atoms in the 2H MoS₂ phase are decorated at the Mo and S edges, generating a K-decorated 2H MoS₂ phase. The uniform atomic distributions of K over the 1T' MoS₂ phase and 2H MoS₂ species were also evidenced by the mapping HAADF-STEM images (Figure 6).

The origin, influencing factors, and mechanism of phase transformation

The knowledge of the mechanism of phase transformation from oxides to sulfide under the thermally driven kinetics is beneficial to the controllable synthesis of the K-intercalated 1T' MoS₂ and K-decorated 2H MoS₂ phases. The variation of the phase behavior of MoS₂ under the assistance of K was investigated by *in-situ* vulcanization of the unsupported monoclinic K₂MoO₄ species with different thermal annealing temperatures in H₂S/H₂ mixtures. The vulcanization temperatures varied from 20 to 400°C with an appropriate temperature interval (20, 80, 160, 180, 200, 220, 240, 280, 320, 360, and 400°C). Powder X-ray diffraction (PXRD) was used to investigate the evolution of the phase structure of K₂MoO₄ during the vulcanization process. Figure 7 shows the XRD patterns and photograph of the oxidized sample and the sample sulphided at different temperatures. The diffraction peaks of the calcined samples in Figure 7 are assigned to the monoclinic K₂MoO₄ phase (JCPDS card No. 29-1021) with a space group of I2/m(12). After vulcanizing the oxidized sample at 20°C for 2 h, the crystal phases are changed significantly, wherein the K₂MoO₄ phase weakens, and three complex crystal phase structures appears, including the orthorhombic K₂MoO₂S₂ structure with space group Pnma (62) (JCPDS card No. 23-1355), the tetragonal K$_{1.0}$MoO₄ structure (JCPDS card No. 21-1293) with space group of P41, 3212 (92), and the monoclinic K₂S₂O₇ with space group of C2/c(15) structure (JCPDS card No. 22-1239). In the first category, the appearance of K₂MoO₂S₂ oxysulfide suggests that H₂S molecules can attack O in K₂MoO₄ oxide to induce a strong chemical reaction, even at the atmosphere temperature. This process is defined as Mars-van Krevelen-like mechanism owing to the
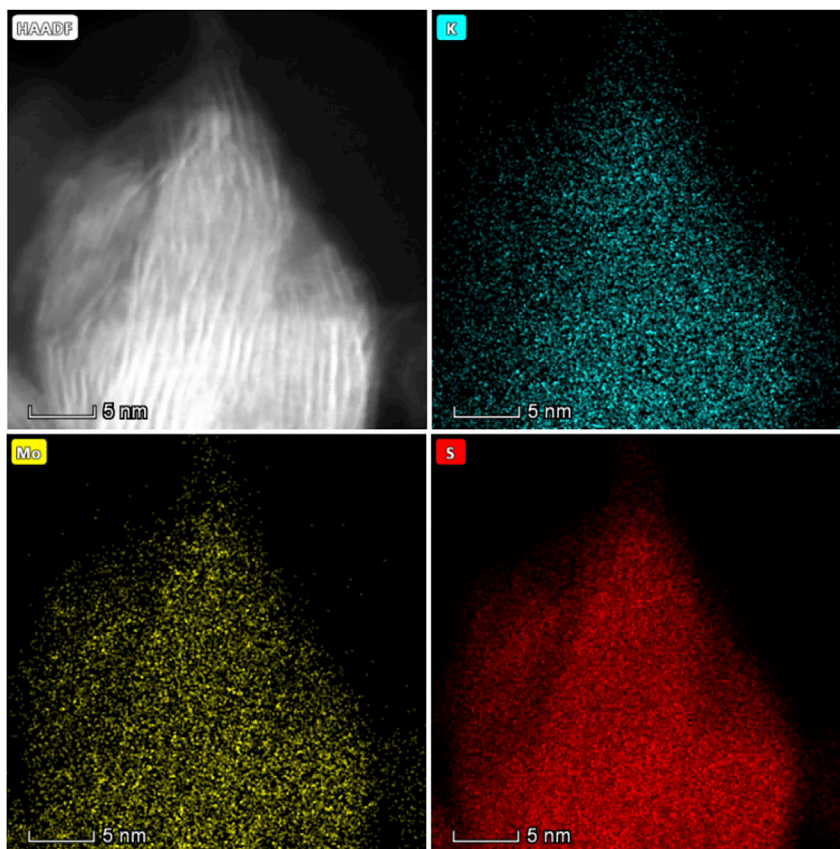
Figure 6. The STEM-EDX mappings of K-Mo/MS catalyst sulphided at 320°C

generation of $K_2MoO_2S_2$, named the O-S exchange mechanism, and we proved herein that this process could occur at room temperature. The observed yellow sample in Figure 7B also proves that the O-S exchange mechanism occurs. For the second category, the tetragonal $K_{1.0}MoO_4$ and monoclinic $K_2S_2O_7$ structures are not common in the reported literature, and the appearance of those two phases indicates that the H_2S molecule promotes the separation of K species from the K_2MoO_4. These results show that the complex phase transition and phase separation behavior could occurr even at room temperature.

When the vulcanization temperatures are increased to 80, 160, and 180°C, respectively, the overall crystal phase structures do not change distinctly, followed by the enhanced diffraction intensity owing to the increased crystallinity. Within this temperature range, two new crystalline phases also appear, the orthogonal K_2MoOS_3 structure with the space group of Pnma (62) (JCPDS card No. 23-1356) and monoclinic $K_2S_4O_6$ structure with the space group of C*/c(15) (JCPDS card No. 02-0441). The appearance of K_2MoOS_3 and $K_2S_4O_6$ indicates that the degree of vulcanization increases with increasing temperature. As the sulfidation temperature continues to increase, the crystalline phase begins to change dramatically. When the vulcanization temperature arrives at 200°C, all the above-mentioned crystal phases gradually disappear, new amorphous structures begin to form. When the vulcanization temperature is increased to 220, 240, or 280°C, respectively, two new crystal phase structures are formed, i.e., an octahedral $K_{1.0}MoS_2$ structure (JCPDS card No. 18-1064) and a hexagonal K_2SO_4 structure with the space group of P63 mc (186) (JCPDS card No. 25-0681). These results show that the orthocrystalline $K_2MoO_2S_2$ and K_2MoOS_3 oxysulfides are completely sulphided into the $K_{1.0}MoS_2$ phase in the temperature range of 220-280°C. The critical temperature for the phase transition from the oxidized state to the sulfurized state is 200°C in a H_2S/H_2 atmosphere. After the vulcanization temperature is further increased to above 320°C, the K_2SO_4 phase is completely decomposed, and the decomposed K ions are inserted into the middle of the layers of MoS_2 phase to generate more $K_{1.0}MoS_2$, namely K-intercalated MoS_2 phase. In addition, some incomplete sulfidation of K_2MoO_4 is existed during the entire temperature range owing to the bulk
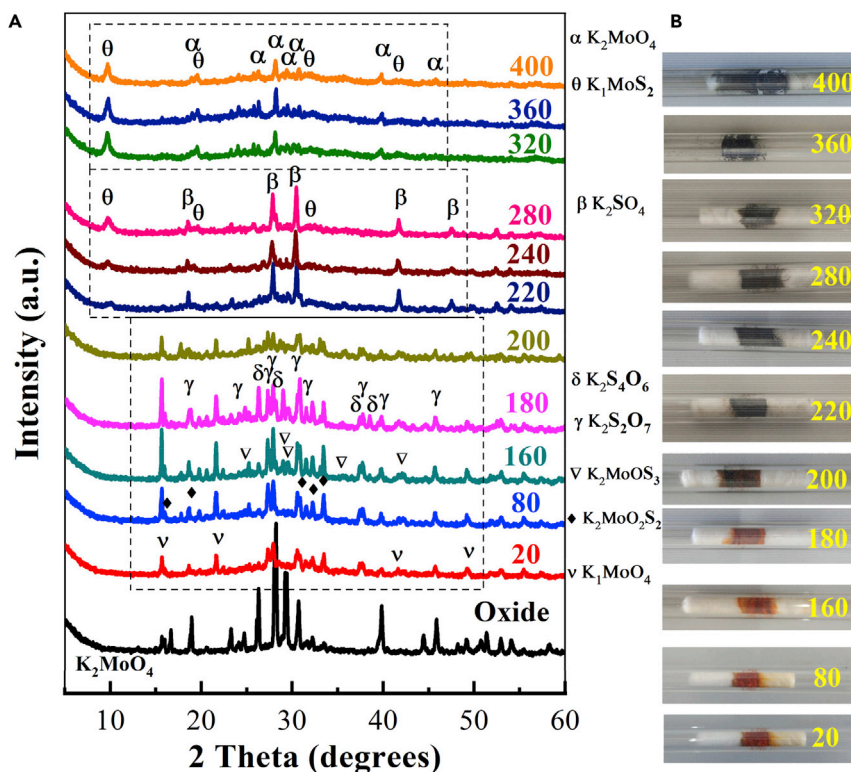
Figure 7. XRD profiles of bulk K$_2$MoO$_4$

(A) XRD profiles and (B) the picture of macroscopic color changes over bulk K$_2$MoO$_4$ and the corresponding oxides sulphided at different temperatures (20, 80, 160, 180, 200, 220, 240, 280, 320, 360, and 400°C). The number of temperature is represented by the sample of K$_2$MoO$_4$ sulphided at the corresponding temperature.

property of oxide precursor. The color change diagram of the real object also matches the critical temperature of the crystal structure transition. It can be concluded that during the vulcanization process, the phenomenon of phase transitions and phase separation is observed owing to the occurrence of O-S replacement, and the K-inserted MoS$_2$ phase is, eventually, formed. All of the above-mentioned species and the corresponding phase transformations from oxide to sulfide are also demonstrated by Raman and XPS characterizations (see Figures S2, S3, and S4).

It should be noted that when the bulk oxide is sulfurized at 400°C, there is the dominance of K-intercalated 1T' MoS$_2$ phase presented in the sample of 400-B as confirmed by Raman (Figure 8), while the supported sample sulfurized at the same temperature shows the presence of a large amount of K-decorated 2H MoS$_2$ phase in the sample of 400-S (Figure 8), indicating that metal-support interaction plays an important role in the phase transformation between 2H MoS$_2$ and 1T' MoS$_2$ phases. Because of strong metal-support (Mo-Si) interactions, the 1T' MoS$_2$ phase trends to be converted into 2H MoS$_2$ species. Based on the above phenomenon, the K species, thermal annealing temperature, and the metal-support interaction are the key factors that affect the phase transformation between K-decorated 2H MoS$_2$ and K-intercalated 1T' MoS$_2$ phases.

The investigation of the structure-performance relationship

The supported catalysts sulphided at different temperatures were used to evaluate the catalytic activity using a fixed-bed reactor. To exclude the effect of the difference between the reaction pressure and the characterization pressure on recognizing the real active phase, we performed the reaction of CH$_3$SH synthesis at atmosphere pressure as same as the pressure used for XPS characterization. The structure-property relationships were established according to the activity data (conducted at 280°C) as well as the amount of K-decorated 2H MoS$_2$ and K-intercalated 1T' MoS$_2$ phases (calculated based on the XPS data). Figure 9 shows the relationships between the reaction rate of CO (R$_{CO}$) and the formation rate of
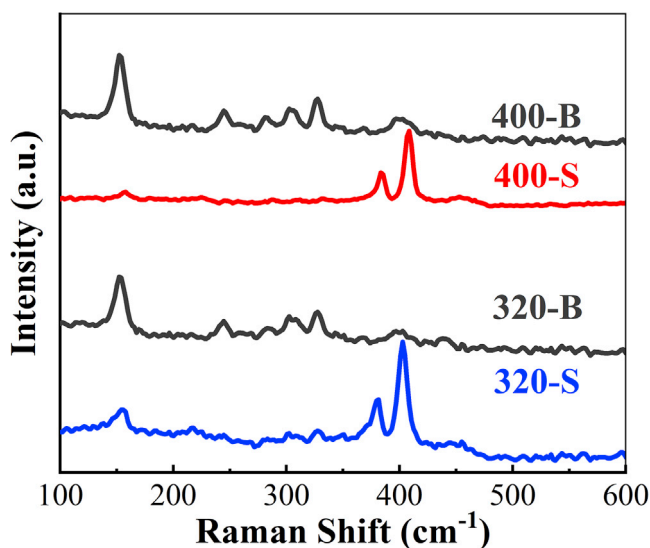
Figure 8. Raman spectra of sulfided samples: bulk K$_2$MoO$_4$ sulphided at 320°C and 400°C (320-B and 400-B), respectively, as well as K$_2$MoO$_4$ supported on MS samples sulphided at 320 and 400°C (320-S and 400-S), respectively

CH$_3$SH (R$_{CH3SH}$) with the amount of K-decorated 2H MoS$_2$ and K-intercalated 1T' MoS$_2$ phases. It is found that when the amount ratio of the K-intercalated 1T' MoS$_2$ phase increases, the values of R$_{CO}$ and R$_{CH3SH}$ increase linearly, revealing that K-intercalated 1T' MoS$_2$ phases are the active phases in the synthesis of CH$_3$SH. On the other hand, when the amount ratio of K-decorated 2H MoS$_2$ phase increases, the values of R$_{CO}$ and R$_{CH3SH}$ decrease, not linearly, in the form of power exponents. When the amount of K-decorated 2H MoS$_2$ phase increases to an infinite value, the values of R$_{CO}$ and R$_{CH3SH}$ will arrive a steady-state numerical values. This result also proves that K-decorated 2H MoS$_2$ phase also possesses a certain level of catalytic activity. Unfortunately, it is unknown which kinds of active phases have higher catalytic performance for the synthesis of CH$_3$SH, and the direct comparison of the catalytic activity of those two MoS$_2$-based phases is lacking in the current literature, which leads to the difficulty in designing the high-performance catalysts (Cordova et al., 2015; Lu et al., 2020b; Yu et al., 2020). A quantitative analysis was performed to solve this issue. When sulphided at 400°C, the relative amount ratio of K-decorated 2H MoS$_2$ is as high as 0.03 with a low relative amount ratio of K-intercalated 1T' MoS$_2$ of 0.007, while when sulphided at 280°C, the corresponding relative amount ratio of K-decorated 2H MoS$_2$ decreases to 0.0025 with an increased amount ratio of K-intercalated 1T' MoS$_2$ of 0.033. At this time, the values of R$_{CO}$ and R$_{CH3SH}$ for the sample sulphided at 400°C are 1.19*10^{-3} mol$_{CO}$mol$^{-1}_{Mo}$s^{-1} and 1.77*10^{-4} mol$_{CH3SH}$mol$^{-1}_{Mo}$s^{-1}, respectively, while the corresponding values for the sample sulphided at 280°C increase to 2.34*10^{-3} mol$_{CO}$mol$^{-1}_{Mo}$s^{-1} and 3.69*10^{-4} mol$_{CH3SH}$mol$^{-1}_{Mo}$s^{-1}, respectively. These results clearly demonstrate that the K-intercalated 1T' MoS$_2$ phase has higher catalytic performances than that of the K-decorated 2H MoS$_2$ phase.

H$_2$-TPR experiments were conducted to uncover the underlying causes why K-intercalated 1T' MoS$_2$ phases are the most active phase. Our previous research results showed that active sulfur species had important role in the synthesis of CH$_3$SH (Lu et al., 2020a). Thus, the property and amount of active sulfur species over MoS$_2$-based catalysts were investigated by H$_2$-TPR and the results were shown in Figure 10. It is observed that the small reduction peak between 500 and 600°C is assigned to K$_2$S or K$_2$SO$_3$/K$_2$SO$_4$ species (Lu et al., 2020a). Importantly, two main reduction peaks are presented between 300 and 400°C, and distinct variation in reduction peak intensity is found. The intensity of low-temperature peak attributed to high-active sulfur gradually decreases with the increased sulphided temperature, while the intensity of medium-temperature peak assigned to low-active sulfur, instead, increases. Combined the sulfur intensity variation in H$_2$-TPR with the quantitative result of XPS (Figure 2A), the amount of surface low-temperature reactive sulfur and medium-temperature reactive sulfur species are found to have a certain correlation with the amount of K-intercalated 1T' MoS$_2$ and K-decorated 2H MoS$_2$ phases, as established in Figures 10B and 10C, respectively. These well-correlated results indicate that the reduction peak in the low-temperature region
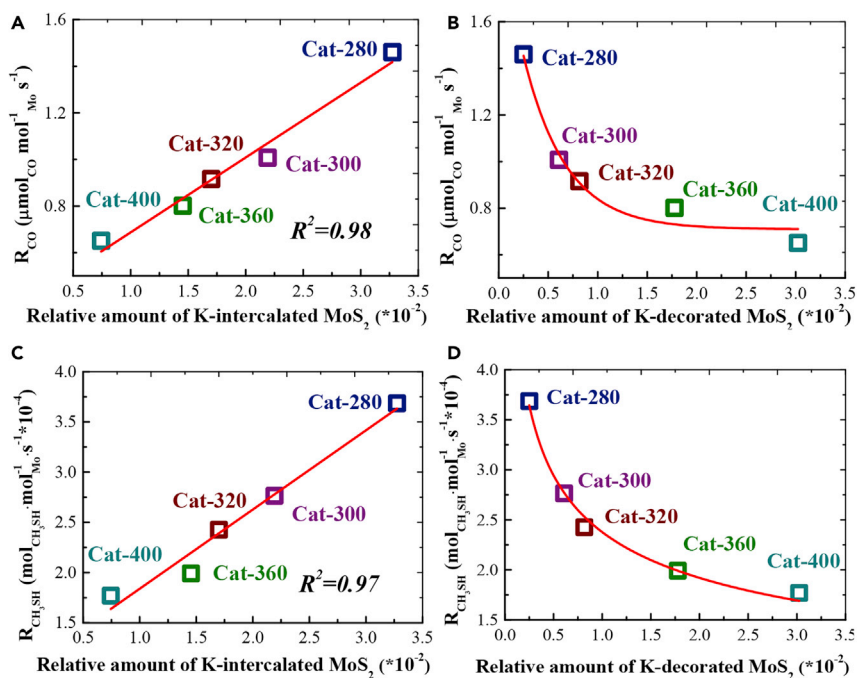
Figure 9. The profiles of structure-performance correlationships

Correlationships between the reaction rate of CO and the relative amount of K-intercalated 1T'-MoS₂ (A) and K-decorated 2H-MoS₂ (B), respectively. Correlationships between the formation rate of CH₃SH and the relative amount of K-intercalated 1T'-MoS₂ (C) and K-decorated 2H-MoS₂ (D), respectively. All the relative amount of above K-Mo species were calculated by the molar ratio of Mo/Si based on XPS analysis.

is related to reactive sulfur species in the K-intercalated 1T' MoS₂, and the reduction peak in a medium temperature region is associated with reactive sulfur species in the K-decorated 2H MoS₂ phase. It is obvious that the sulfurs in the basal plane of K-intercalated 1T' MoS₂ are activated and have higher active than that of K-decorated 2H MoS₂ (Yu et al., 2018). With the intercalation of K into the layers of 2H-MoS₂, the coordination mode of MoS₂ is transferred from a trigonal prismatic to the octahedral structure, forming 1T'-MoS₂. The change in the coordination form of S around Mo drastically alters the activity of surface sulfur owing to the electronic influence (as revealed by the variation in the binding energy of Mo 2p XPS spectra by 0.7 eV between 2H and 1T'-MoS₂ in Figure 2A) and the spatial behavior of K (as confirmed by the enlarged interlayer spacing by 0.27 nm in Figure 3). In combination with the previous correlation between the amount of active MoS₂ phases and the activity results, it is determined that the reactive sulfur in K-intercalated 1T' MoS₂ phases is the most active species for the synthesis of CH₃SH from CO/H₂/H₂S (see Figure S5, 9, and 10). As for surface sulfur species in K-decorated 2H MoS₂ phases, as shown in Figure 10C, a non-linear relationship is established where when the amount of K-decorated 2H MoS₂ gradually increases, the amount of surface sulfur species increases at first and then plateaus. This result evidences that when the vulcanizing temperature increases, the surface sulfur species in K-decorated 2H MoS₂ phase are gradually converted into strongly bonded sulfur species that cannot be detected in the temperature range of TPR procedure, which in turn decreases the catalytic activity. It is also possible that the low activity of K decorated 2H-MoS₂ is owing to that K atoms occupy the Mo-CUS on the surface of MoS₂, thus resulting in decreased surface active sites and lower activity. However, our previous study proved that when the catalytic properties of MoS₂/SBA-15 and K-MoS₂/SBA-15 were compared, MoS₂/SBA-15 with larger Mo-CUS had lower activity, thus excluding the above cause. Therefore, it is concluded that the surface reactive sulfur species located in the environment of K-intercalated 1T' MoS₂ phase has higher catalytic performances than that of surface sulfur species located in the environment of the K-decorated 2H MoS₂ phase.

For the synthesis of CH₃SH, it is generally accepted that the reaction of CO and H₂S first promotes the formation of C-S bond, and the subsequent hydrogenation of C-S bond facilitates the generation of CH₃SH (Gutiérrez et al., 2011a; Lu et al., 2020a). In our precious researches, the formation and stabilization of C-S
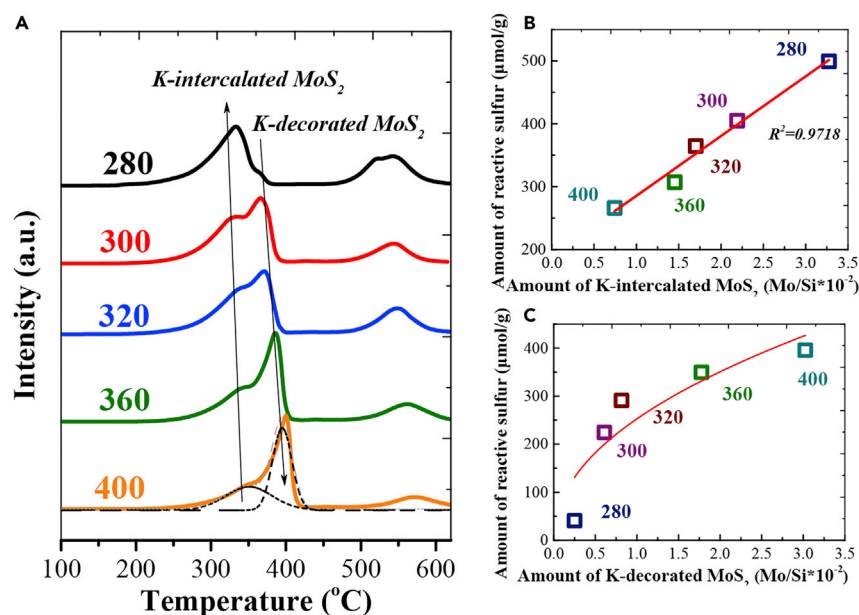
Figure 10. H$_2$-TPR results of K-Mo/MS catalysts

H$_2$-TPR results (A) of K-Mo/MS catalysts sulphided at 280, 300, 320, 360, and 400°C, respectively. The amount of reactive sulfur species was plotted as a function of amount of K-intercalated 1T'-MoS$_2$ (B) and K-decorated 2H-MoS$_2$ (C), respectively (detected by XPS).

bond were reported to be fundamental to synthesizing CH$_3$SH from the molecules of CO and H$_2$S with the aid of H$_2$ (Lu et al., 2020a). Tuning the binding strength of C-S bond to the moderate degree, represented by the strength of the Mo-S bond over MoS$_2$, was found to be the key factor for the stabilization of C-S bond in the intermediate and final product of COS and CH$_3$SH (Lu et al., 2020a, 2020b). Too strong the strength of Mo-S bond would lead to the rupture of C-S bond in absorbed intermediate species. The previous study showed that the strong strength of Mo-S bond over K-Mo-based catalysts reflected by the reduction temperature of about 400°C in H$_2$-TPR greatly inhibits the formation of CH$_3$SH (Lu et al., 2020a). In our current work, the H$_2$-TPR result shows that K-decorated MoS$_2$ has the strong strength of Mo-S bond, as reflected by the reduction temperature of about 400°C, which leads to the lower catalytic performance for the synthesis of CH$_3$SH. In contrast, K-intercalated MoS$_2$ exhibits the moderate strength of Mo-S bond, as reflected by the reduction temperature of about 350°C, which is in favor of stabilizing the C-S bond and facilitating the generation of CH$_3$SH.

As adsorption is an essential stage of catalysis, the difference in the adsorption and desorption properties of reactants is further considered to reveal the cause for the higher performance of K-intercalated MoS$_2$ than K-decorated MoS$_2$. Temperature-programmed desorption (TPD) of CO, H$_2$, and H$_2$S were shown in Figures 11A and 11B, and 11(C), respectively. There are three CO desorption peaks in Figure 11A, indicating the presence of three kinds of adsorption behaviors. As reported in the literature, the first desorption peak is typically assigned to the physisorbed CO, and the desorption peak at high temperature of about 700°C is attributed to the strongly chemisorbed CO, as well as the moderate temperature peak corresponds to the desorption of CO linked with hydrogen bond over -SH group (Aegerter et al., 1996; Li et al., 1992; Zhang et al., 1998). Distinctly, the desorption of H$_2$S has a similar behavior to CO, indicating that CO has similar adsorption sites to H$_2$S. It is clear that the sample sulphided at 280°C with the domination of K-intercalated MoS$_2$ shows the presence of far larger amount of strongly chemisorbed CO as well as H$_2$S than that of the sample sulphided at 400°C with the domination of K-decorated MoS$_2$. This result suggests that K-intercalated MoS$_2$ has stronger ability for chemically bonding CO and H$_2$S to form and stabilize the C-S bond. As for K-decorated MoS$_2$ over the sample sulphided at 400°C, there is no presence of desorbed H$_2$S at high temperature, indicating a certain amount of H$_2$S adsorbed in the K-Mo sample cannot be desorbed during the desorption temperature range of TPD owing to the over-strong Mo-S bond strength (as seen in Figure 10). Notably, the existence of strongly chemisorbed H$_2$S over K-decorated MoS$_2$ can be confirmed in the literature owing to the strong nucleophilicity of H$_2$S with MoS$_2$ (Zhang et al., 1998).
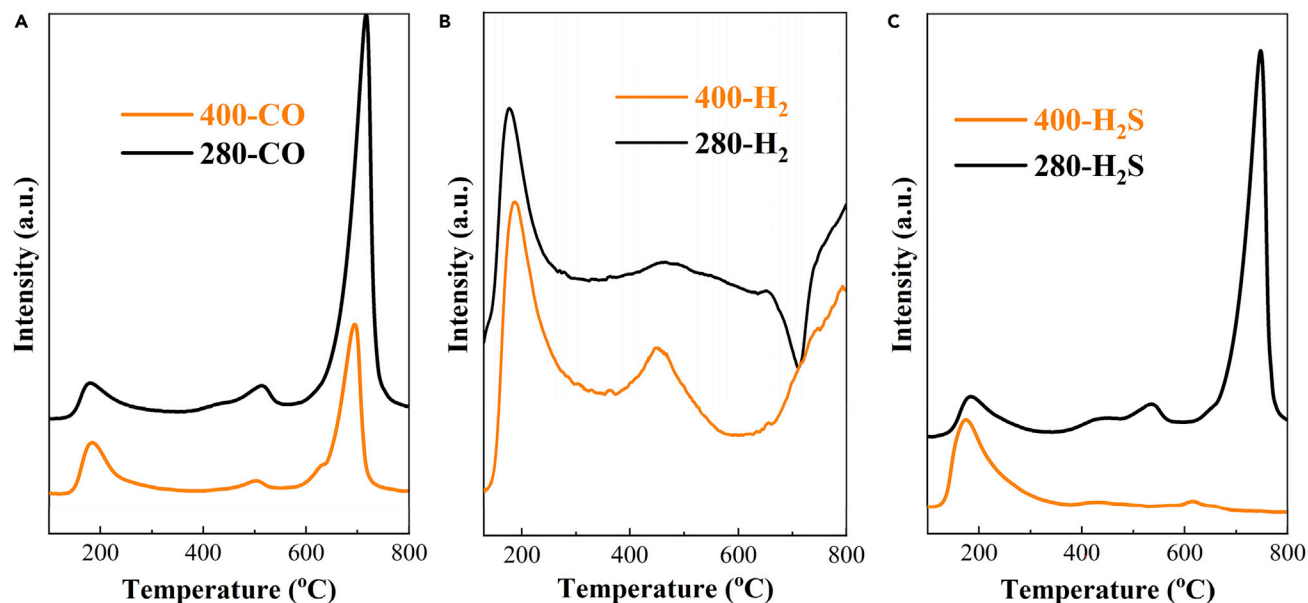
Figure 11. TPD curves of K-Mo/MS catalysts
TPD curves of CO (A), H_2 (B), and H_2S (C) over K-Mo/MS catalysts sulphided at 280 and 400°C, respectively.

Moreover, the adsorption and desorption behavior of H_2 over K-intercalated MoS_2 and K-decorated MoS_2 are different from that of CO and H_2S, suggesting the adsorption sites of H_2 is not the same as that of CO and H_2S. The difference possibly explains the mechanism for the synthesis of CH_3SH. It is observed that the low-temperature desorption peak at about 200°C is assigned to the physically adsorbed H_2, and large amount of desorbed H_2 at moderate temperature is generated over K-decorated MoS_2, but not for K-intercalated MoS_2, which is originated from the chemically adsorbed H_2. Distinctly, the desorption of H_2 over K-decorated MoS_2 detected by TCD is activated as the hydrogen molecule. However, there is a distinct negative peak of H_2 over K-intercalated MoS_2, suggesting the consumption of H_2 and the possible dissociation of H_2 into adsorbed H^* or the reaction of high-active sulfur with H_2 (see Figure S6). However, in fact, the reaction of H_2 with the high active S species over MoS_2 generally requires the occurrence of the heterolytic and homolytic dissociation of H_2 into adsorbed H^*, as proved by the experimental evidence and DFT calculations (Afanasiev and Jobic, 2021; L. Jalowiecki et al., 1990; Li et al., 1992). All the results indicate, when the C-S bond is formed, if H_2 is activated as the hydrogen molecule, the attack of C-S bond by the hydrogen molecule easily leads to the cleavage of the C-S bond, as confirmed by the hydro-desulfurization of thiophene over $CoMoS_2$ based catalysts (Chouzier et al., 2011). On the contrary, the C-S bond shows enough nucleophilicity with the adsorbed H^*, the intimate contact of the C-S bond with adsorbed H^* easily stabilizes the C-S bond and promotes the hydrogenation to generate adsorbed CH_3SH^* (Li et al., 1992).

It should be noted that there are several questions in dispute presented in the current literature. The theoretical analysis in the literature considers that the layer gap of the 1T(1T') MoS_2 phase has higher steric hindrance for intermediates than that of the 2H MoS_2 phase (Lu et al., 2020b), and thus the 1T(1T') MoS_2 phase is regarded as a lower catalytic activity species. However, the reaction for the synthesis of CH_3SH from CO/H_2/H_2S more easily occurs at the external surface of K-MoS_2 phases, rather than the layer gap of K-MoS_2, which discounts the conclusion. In this reported literature, the higher dispersion of K-MoS_2 species seems to be the main reason for the higher catalytic performance. Also, a recent study by Hensen et al. prepared the K-Mo catalysts with pure 1T MoS_2 species and found that when the K-Mo catalysts were performed at 350°C and 10 bar, the 1T MoS_2 species had a tendency to convert into 2H MoS_2 species and was regarded to have no correlation with the generation of CH_3SH (Yu et al., 2020). However, our experiments were conducted at 280°C under atmospheric pressure, so the mild reaction conditions guaranteed that the catalytic activity of the 1T' MoS_2 species remained relatively stable within 5 h test (Figures S7 and S8), and the 1T' MoS_2 phase survived during the reaction as detected by XRD (Figure S9). The differences in the stability between our experiment and literature might be owing to the following reasons. The first one is owing

to the property difference between the 1T MoS$_2$ and 1T' MoS$_2$ species. This 1T' MoS$_2$ phase is a distorted octahedral structure and is usually originated from the distortion of the octahedral 1T structure in such a way as to generate Z chains of bonded Mo-Mo atoms (Gao et al., 2015; Zhang et al., 2016). Actually, the pure 1T structure has a formation energy of 0.84 eV, while the 1T' MoS$_2$ species has a lower formation energy of 0.55 eV, which shows the difference in the stability. As largely reported in the literature, the 1T' MoS$_2$ species was reported to have higher stability than typical trigonal 2H K$_{0.4}$MoS$_2$ and pure octahedral 1T MoS$_2$ (Qian et al., 2014; Wang et al., 2013; Zhang et al., 2016). Therefore, it is reasonable that K-intercalated 1T' MoS$_2$ species in our work exhibit higher stability especially under conditions of low temperature and room pressure. Furthermore, a recent study found that the stability of 1T' MoS$_2$ was related to the increased concentration of K, i.e., the 1T' species became even more stable than the 2H phase when the K concentration exceeded 44% (Liu et al., 2018). The higher theoretical content of K in our work (10.8 wt%) than that of 5.5 wt% that reported in the literature (Yu et al., 2020) explains why the K-intercalated 1T' MoS$_2$ phase has relatively stable catalytic activity in our experiment. More importantly, large number of literature had focused on the development of various strategies to further improve the stability of 1T MoS$_2$ and 1T' MoS$_2$ species, including a one-step hydrothermal method assisted with ammonium ions (Geng et al., 2016; Liu et al., 2015b), a colloidal synthesis method (Mahler et al., 2014), the intercalation of alkali metal (Liu et al., 2018; Tan et al., 2017), the stability by Co and Re (Li et al., 2018; Xia et al., 2018), surface covalent functionalization (Tang and Jiang, 2015), injecting the negative charge (Gao et al., 2015), and constructing interfacial engineering (Liu et al., 2017; Nasr Esfahani et al., 2015). For example, the transition of 2H MoS$_2$ into the metallic 1T MoS$_2$ phase under a high pressure of 35 GPa proved the achievement of the improvement in the stability of 1T MoS$_2$ phase at a relatively low temperature and a specific pressure (Geng et al., 2016). Considering the excellent properties of 1T' MoS$_2$ in the activation of surface sulfur species at the basal plane, K-intercalated 1T' MoS$_2$ had good potential application in low-temperature catalysis (Chang et al., 2016; Zhang et al., 2016).

Conclusion

In summary, we controllably synthesized two phases, K-intercalated 1T' MoS$_2$ and K-decorated 2H MoS$_2$, via phase engineering with a simple K-induced thermally driven tuning method. The phase transformation of 2H MoS$_2$ from/to 1T' MoS$_2$ depended strongly on the presence of K, the annealing vulcanizing temperature, and the metal-support interaction. The precise position and atomic distribution of K over the MoS$_2$ phase were evidenced at the atomic level via the HADDF-STEM technique. One K position-dependent catalytic activity was found, where when K was located in the gaps of MoS$_2$ layers, K-intercalated 1T' MoS$_2$ was formed, which had linear correlations with the catalytic performance for the synthesis of CH$_3$SH. However, when K was located at the edge of MoS$_2$, K-decorated 2H MoS$_2$ was generated, which exhibited a lower catalytic activity than that of intercalated species. The origin of the excellent catalytic performances for the synthesis of CH$_3$SH over K-intercalated 1T' MoS$_2$ was owing to the K activation of surface insert sulfur induced by the K position-dependent phase transition, which gave rise to the marked differences in the adsorption and activation of CO, H$_2$S, and H$_2$ molecules as well as in the stabilization of C-S intermediate. K-intercalated 1T' MoS$_2$ had a strong ability to adsorb CO and H$_2$S so as to stabilize the C-S bond, then the activation of H$_2$ as adsorbed H* led to the hydrogenation of C-S bond into CH$_3$SH*. The confirmation of the K position, characteristic and catalytic behavior as well as phase transformation behavior of K-induced 2H-MoS$_2$ from/to 1T(T')-MoS$_2$ could provide theoretical direction for the synthesis of CH$_3$SH.

Limitations of the study

In this work, although K-intercalated 1T' MoS$_2$ was demonstrated to have high catalytic activity and selectivity to CH$_3$SH. The stability of this phase still needed to be further improved by exploiting new methods in the future. In addition, more evidences of *in situ* XPS and *in situ* DRIFTS are needed to further strengthen the phase transformation and reaction mechanism in future work.

Supporting citations

The following references appear in the Supplemental information: Paraguassu et al., 2012; Saraiva et al., 2012; Vilchez and Griffith, 1972; Schmidt and Müller, 1974; Schrader and Cheng, 1983; Schmidt and Müller, 1972; Liang et al., 2015; Wang et al., 2014b; Wang et al., 2016; Voiry et al., 2013a; Erdohelyi et al., 1997; Bao et al., 2015; Muijsers et al., 1995; Sgroi et al., 2014; Weber et al., 1996; Benoist et al., 1995; Hui et al., 2008; Wang et al., 2018; Bao et al., 2015; Benoist et al., 1994; Seifert et al., 1980.

STAR★METHODS

Detailed methods are provided in the online version of this paper and include the following:

- KEY RESOURCES TABLE
- RESOURCE AVAILABILITY
  - Lead contact
  - Materials availability
  - Data and code availability
- METHOD DETAILS
  - Catalyst preparations
  - Characterizations of the catalysts
  - Catalytic performance evaluation
- QUANTIFICATION AND STATISTICAL ANALYSIS

SUPPLEMENTAL INFORMATION

Supplemental information can be found online at https://doi.org/10.1016/j.isci.2022.104999.

AUTHOR CONTRIBUTIONS

J. Lu and Y. Luo conceived the idea and analyzed the data. J. Fang and Z. Xu prepared the catalysts and conducted catalytic reactions. The researcher of www.ceshigo.com and J. Lu performed the STEM measurements. Z. Xu, D. He, S. He, and J. Fang conducted other characterizations and anticipated discussion. Y. Luo supervised the project, helped design the experiments, and analyzed the data. Z. Xu and J. Lu wrote the article. All the authors commented on the article and have given approval to the final version of the article.

DECLARATION OF INTERESTS

The authors declare no competing interests.

REFERENCES

Aegerter, P.A., Quigley, W.W., Simpson, G.J., Ziegler, D.D., Logan, J.W., McCrea, K.R., Glazier, S., and Bussell, M.E. (1996). Thiophene hydrodesulfurization over alumina-supported molybdenum carbide and nitride catalysts adsorption sites, catalytic activities, and nature of the active surface. J. Catal. 164, 109–121.

Afanasiev, P., and Jobic, H. (2021). On hydrogen adsorption by nanodispersed MoS₂-based catalysts. J. Catal. 403, 111–120. https://doi.org/10.1016/j.jcat.2020.12.020.

Andersen, A., Kathmann, S.M., Lilga, M.A., Albrecht, K.O., Hallen, R.T., and Mei, D. (2011). Adsorption of potassium on MoS₂(100) surface: a first-principles investigation. J. Phys. Chem. C 115, 9025–9040. https://doi.org/10.1021/jp110069r.

Bai, B., and Li, J. (2014). Positive effects of K⁺ ions on three-dimensional mesoporous AgCo₃O₄ catalyst for HCHO oxidation. ACS Catal. 4, 2753–2762. https://doi.org/10.1021/cs5006663.

Bao, X.Q., Petrovykh, D.Y., Alpuim, P., Stroppa, D.G., Guldris, N., Fonseca, H., Costa, M., Gaspar, J., Jin, C., and Liu, L. (2015). Amorphous oxygen-rich molybdenum oxysulfide decorated p-type silicon microwire arrays for efficient photoelectrochemical water reduction. Nano Energy 16, 130–142. https://doi.org/10.1016/j.nanoen.2015.06.014.

Benoist, L., Gonbeau, D., Pfister-Guillouzo, G., Schmidt, E., Meunier, G., and Levasseur, A. (1994). XPS analysis of lithium intercalation in thin films of molybdenum oxysulphides. Surf. Interface Anal. 22, 206–210.

Benoist, L., Gonbeau, D., Pfister-Guillouzo, G., Schmidt, E., Meunier, G., and Levasseur, A. (1995). X-ray photoelectron spectroscopy characterization of amorphous molybdenum oxysulfide thin films. Thin Solid Films 258, 110–114.

Chang, K., Hai, X., Pang, H., Zhang, H., Shi, L., Liu, G., Liu, H., Zhao, G., Li, M., and Ye, J. (2016). Targeted synthesis of 2H- and 1T-phase MoS₂ monolayers for catalytic hydrogen evolution. Adv. Mater. 28, 10033–10041. https://doi.org/10.1002/adma.201603765.

Chen, A., Wang, Q., Li, Q., Hao, Y., Fang, W., and Yang, Y. (2008). Direct synthesis of methanethiol from H₂S-rich syngas over sulfided Mo-based catalysts. J. Mol. Catal. Chem. 283, 69–76. https://doi.org/10.1016/j.molcata.2007.12.014.

Cheng, Y., Nie, A., Zhang, Q., Gan, L.-Y., Shahbazian-Yassar, R., and Schwingenschlogl, U. (2014). Origin of the phase transition in lithiated molybdenum disulfide. ACS Nano 8, 11447–11453.

Chouzier, S., Vrinat, M., Cseri, T., Roy-Auberger, M., and Afanasiev, P. (2011). HDS and HDN activity of (Ni, Co)Mo binary and ternary nitrides prepared by decomposition of hexamethylenetetramine complexes. Appl. Catal. Gen. 400, 82–90. https://doi.org/10.1016/j.apcata.2011.04.023.

Cordova, A., Blanchard, P., Lancelot, C., Frémy, G., and Lamonier, C. (2015). Probing the nature of the active phase of molybdenum-supported catalysts for the direct synthesis of methylmercaptan from syngas and H2S. ACS Catal. 5, 2966–2981. https://doi.org/10.1021/cs502031f.

Cordova, A., Blanchard, P., Salembier, H., Lancelot, C., Frémy, G., and Lamonier, C. (2017). Direct synthesis of methyl mercaptan from H2/CO/H2S using tungsten based supported catalysts: investigation of the active phase. Catal. Today 292, 143–153. https://doi.org/10.1016/j.cattod.2016.10.032.

Dai, X., Li, Z., Du, K., Sun, H., Yang, Y., Zhang, X., Ma, X., and Wang, J. (2015). Facile synthesis of in–situ nitrogenated graphene decorated by few–layer MoS2 for hydrogen evolution reaction. Electrochim. Acta 171, 72–80. https://doi.org/10.1016/j.electacta.2015.05.017.

Eda, G., Yamaguchi, H., Voiry, D., Fujita, T., Chen, M., and Chhowalla, M. (2011). Photoluminescence from chemically exfoliated MoS2. Nano Lett. 11, 5111–5116. https://doi.org/10.1021/nl201874w.

Erdohelyi, A.F., Fodor, K., and Solymosi, F. (1997). Partial oxidation of methane on supported potassium molybdate. J. Catal. 166, 244–253.

Gao, G., Jiao, Y., Ma, F., Jiao, Y., Waclawik, E., and Du, A. (2015). Charge mediated semiconducting-to-metallic phase transition in molybdenum disulfide monolayer and hydrogen evolution reaction in new 1T′ phase. J. Phys. Chem. C 119, 13124–13128. https://doi.org/10.1021/acs.jpcc.5b04658.

Geng, X., Sun, W., Wu, W., Chen, B., Al-Hilo, A., Benamara, M., Zhu, H., Watanabe, F., Cui, J., and Chen, T.-p. (2016). Pure and stable metallic phase molybdenum disulfide nanosheets for hydrogen evolution reaction. Nat. Commun. 7, 10672. https://doi.org/10.1038/ncomms10672.

Goki Eda, T.F., Fujita, T., Yamaguchi, H., Voiry, D., Chen, M., and Chhowalla, M. (2012). Coherent atomic and electronic heterostructures of single-layer MoS2. ACS Nano 6, 7311–7317.

Gutiérrez, O.Y., Kaufmann, C., Hrabar, A., Zhu, Y., and Lercher, J.A. (2011a). Synthesis of methyl mercaptan from carbonyl sulfide over sulfide K2MoO4/SiO2. J. Catal. 280, 264–273. https://doi.org/10.1016/j.jcat.2011.03.027.

Gutiérrez, O.Y., Kaufmann, C., and Lercher, J.A. (2011b). Influence of potassium on the synthesis of methanethiol from carbonyl sulfide on sulfided Mo/Al2O3 catalyst. ChemCatChem 3, 1480–1490. https://doi.org/10.1002/cctc.201100124.

Gutiérrez, O.Y., Kaufmann, C., and Lercher, J.A. (2011c). Synthesis of methanethiol from carbonyl sulfide and carbon disulfide on (Co)K-promoted sulfide Mo/SiO2 catalysts. ACS Catal. 1, 1595–1603. https://doi.org/10.1021/cs200455k.

Hao, Z., Shen, Z., Li, Y., Wang, H., Zheng, L., Wang, R., Liu, G., and Zhan, S. (2019). The role of alkali metal in α-MnO2 catalyzed ammonia-selective catalysis. Angew Chem. Int. Ed. Engl. 58, 6351–6356. https://doi.org/10.1002/anie.201901771.

Hu, Z., Wang, L., Zhang, K., Wang, J., Cheng, F., Tao, Z., and Chen, J. (2014). MoS2 nanoflowers with expanded interlayers as high-performance anodes for sodium-ion batteries. Angew Chem. Int. Ed. Engl. 53, 12794–12798. https://doi.org/10.1002/anie.201407898.

Hui, G., Li, X., Wang, J., Qin, Z., Zhanjun, L., and Yang, Y. (2008). Activation and hydrodesulfurization activity of MoO3/Al2O3 catalyst presulfided by ammonium thiosulfate. Chin. J. Catal. 29, 921–927.

Kong, D., Wang, H., Cha, J.J., Pasta, M., Koski, K.J., Yao, J., and Cui, Y. (2013). Synthesis of MoS2 and MoSe2 films with vertically aligned layers. Nano Lett. 13, 1341–1347. https://doi.org/10.1021/nl400258t.

Jalowiecki, L., Grimblot, J., and Bonnelle, J.P. (1990). Quantitative detection of reactive hydrogen on MoS2/γ-Al2O3 and on γ-Al2O3. J. Catal. 126, 101–108.

Lee, J.S., Kim, S., Lee, K.H., Nam, I.-S., Chung, J.S., Kim, Y.G., and Woo, H.C. (1994). Role of alkali promoters in KMoS2 catalysts for CO-H2 reactions. Appl. Catal. Gen. 110, 11–25.

Li, X., Qian, T., Zai, J., He, K., Feng, Z., and Qian, X. (2018). Co stabilized metallic 1Td MoS2 monolayers: bottom-up synthesis and enhanced capacitance with ultra-long cycling stability. Mater. Today Energy 7, 10–17. https://doi.org/10.1016/j.mtener.2017.11.004.

Li, X., Xin, Q., Guo, X.X., Grange, P., and Delmon, B. (1992). Reversible hydrogen adsorption on MoS2 studied by TemperatureProgrammed desorption and temperature-programmed reduction. J. Catal. 137, 385–393.

Liang, Y., Yoo, H.D., Li, Y., Shuai, J., Calderon, H.A., Robles Hernandez, F.C., Grabow, L.C., and Yao, Y. (2015). Interlayer-expanded molybdenum disulfide nanocomposites for electrochemical magnesium storage. Nano Lett. 15, 2194–2202. https://doi.org/10.1021/acs.nanolett.5b00388.

Ling, C., Ouyang, Y., Shi, L., Yuan, S., Chen, Q., and Wang, J. (2017). Template-grown MoS2 nanowires catalyze the hydrogen evolution reaction: ultralow kinetic barriers with high active site density. ACS Catal. 7, 5097–5102. https://doi.org/10.1021/acscatal.7b01595.

Liu, C., Virginie, M., Griboval-Constant, A., and Khodakov, A.Y. (2016). Potassium promotion effects in carbon nanotube supported molybdenum sulfide catalysts for carbon monoxide hydrogenation. Catal. Today 261, 137–145. https://doi.org/10.1016/j.cattod.2015.07.003.

Liu, C., Wang, L., Tang, Y., Luo, S., Liu, Y., Zhang, S., Zeng, Y., and Xu, Y. (2015a). Vertical single or

few-layer MoS2 nanosheets rooting into TiO2 nanofibers for highly efficient photocatalytic hydrogen evolution. Appl. Catal. B Environ. 164, 1–9. https://doi.org/10.1016/j.apcatb.2014.08.046.

Liu, L., Wu, J., Wu, L., Ye, M., Liu, X., Wang, Q., Hou, S., Lu, P., Sun, L., Zheng, J., et al. (2018). Phase-selective synthesis of 1T′ MoS2 monolayers and heterophase bilayers. Nat. Mater. 17, 1108–1114. https://doi.org/10.1038/s41563-018-0187-1.

Liu, Q., Fang, Q., Chu, W., Wan, Y., Li, X., Xu, W., Habib, M., Tao, S., Zhou, Y., Liu, D., et al. (2017). Electron-Doped 1T-MoS2 via interface engineering for enhanced electrocatalytic hydrogen evolution. Chem. Mater. 29, 4738–4744. https://doi.org/10.1021/acs.chemmater.7b00446.

Liu, Q., Li, X., He, Q., Khalil, A., Liu, D., Xiang, T., Wu, X., and Song, L. (2015b). Gram-scale Aqueous synthesis of stable few-layered 1T-MoS2 applications for visible-light driven photocatalytic hydrogen evolution. Small 11, 5556–5564. https://doi.org/10.1002/smll.201501822.

Lu, J., Fang, J., Xu, Z., He, D., Feng, S., Li, Y., Wan, G., He, S., Wu, H., and Luo, Y. (2020a). Facile synthesis of few-layer and ordered K-promoted MoS2 nanosheets supported on SBA-15 and their potential application for heterogeneous catalysis. J. Catal. 385, 107–119. https://doi.org/10.1016/j.jcat.2020.03.017.

Lu, J., Liu, P., Xu, Z., He, S., and Luo, Y. (2018). Investigation of the reaction pathway for synthesizing methyl mercaptan (CH3SH) from H2S-containing syngas over K-Mo-type materials. RSC Adv. 8, 21340–21353. https://doi.org/10.1039/C8RA03430C.

Lu, J., Luo, Y., He, D., Xu, Z., He, S., Xie, D., and Mei, Y. (2020b). An exploration into potassium (K) containing MoS2 active phases and its transformation process over MoS2 based materials for producing methanethiol. Catal. Today 339, 93–104. https://doi.org/10.1016/j.cattod.2019.01.012.

Mahler, B., Hoepfner, V., Liao, K., and Ozin, G.A. (2014). Colloidal synthesis of 1T-WS2 and 2H-WS2 nanosheets: applications for photocatalytic hydrogen evolution. J. Am. Chem. Soc. 136, 14121–14127. https://doi.org/10.1021/ja506261t.

Muijsers, J.C., Weber, T., Vanhardeveld, R.M., Zandbergen, H.W., and Niemantsverdriet, J.W. (1995). Sulfidation study of molybdenum oxide using MoO3/SiO2/Si(100) model catalysts and Mo3IV-sulfur cluster compounds. J. Catal. 157, 698–705.

Nasr Esfahani, D., Leenaerts, O., Sahin, H., Partoens, B., and Peeters, F.M. (2015). Structural transitions in monolayer MoS2 by lithium adsorption. J. Phys. Chem. C 119, 10602–10609. https://doi.org/10.1021/jp510083w.

Paraguassu, W., Saraiva, G.D., Guerini, S., Freire, P.T.C., Abagaro, B.T.O., and Mendes Filho, J. (2012). Pressure-induced phase transition in K2MoO4: a Raman scattering study and ab initio calculations. J. Solid State Chem. 196, 197–202. https://doi.org/10.1016/j.jssc.2012.06.021.

Qian, X., Liu, J., Fu, L., and Li, J. (2014). Quantum spin Hall effect in two-dimensional transition metal dichalcogenides. Science 346, 1344–1347.

Saraiva, G.D., Paraguassu, W., Freire, P.T.C., Maczka, M., and Filho, J.M. (2012). Temperature-dependent Raman scattering study of K_2MoO_4. Vib. Spectrosc. 58, 87–94. https://doi.org/10.1016/j.vibspec.2011.11.015.

Schmidt, K.H., and Müller, A. (1972). Schwingungsspektren und normalkoordinatenanalyse von $MoOSe_3^{2-}$, $WOSe_3^{2-}$, $MoO_2Se_3^{2-}$, und $WO_2Se_2^{2-}$. Spectrochim. Acta 28, 1829–1840.

Schmidt, K.H., and Müller, A. (1974). Vibrational spectra of transition metal chalcogen compounds. Coord. Chem. Rev. 14, 115–179.

Schrader, G., and Cheng, C.P. (1983). In situ laser Raman spectroscopy of the sulfiding of Mo/Al_2O_3 catalysts. J. Catal. 80, 369–385.

Seifert, G., Finster, J., and Müller, H. (1980). SW Xα calculations and x-ray photoelectron spectra of molybdenum(II) chloride cluster compounds. Chem. Phys. Lett. 75, 373–377.

Sgroi, M., Gili, F., Mangherini, D., Lahouij, I., Dassenoy, F., Garcia, I., Odriozola, I., and Kraft, G. (2014). Friction reduction benefits in valve-train system using IF-MoS_2 added engine oil. Tribol. Trans. 58, 207–214. https://doi.org/10.1080/10402004.2014.960540.

Tan, S.J.R., Abdelwahab, I., Ding, Z., Zhao, X., Yang, T., Loke, G.Z.J., Lin, H., Verzhbitskiy, I., Poh, S.M., Xu, H., et al. (2017). Chemical stabilization of 1T' phase transition metal dichalcogenides with giant optical kerr nonlinearity. J. Am. Chem. Soc. 139, 2504–2511. https://doi.org/10.1021/jacs.6b13238.

Tang, Q., and Jiang, D.E. (2015). Stabilization and band-gap tuning of the 1T-MoS_2 monolayer by covalent functionalization. Chem. Mater. 27, 3743–3748. https://doi.org/10.1021/acs.chemmater.5b00986.

Vilchez, F.G., and Griffith, W.P. (1972). Transition-metal tetra-oxo-complexes and their vibrational spectra. J. Chem. Soc. Dalton Trans. 13, 1416–1421.

Voiry, D., Salehi, M., Silva, R., Fujita, T., Chen, M., Asefa, T., Shenoy, V.B., Eda, G., and Chhowalla, M. (2013a). Conducting MoS_2 nanosheets as catalysts for hydrogen evolution reaction. Nano Lett. 13, 6222–6227.

Voiry, D., Yamaguchi, H., Li, J., Silva, R., Alves, D.C.B., Fujita, T., Chen, M., Asefa, T., Shenoy, V.B., Eda, G., and Chhowalla, M. (2013b). Enhanced catalytic activity in strained chemically exfoliated WS_2 nanosheets for hydrogen evolution. Nat. Mater. 12, 850–855. https://doi.org/10.1038/nmat3700.

Wang, H., Lu, Z., Xu, S., Kong, D., Cha, J.J., Zheng, G., Hsu, P.C., Yan, K., Bradshaw, D., Prinz, F.B., and Cui, Y. (2013). Electrochemical tuning of vertically aligned MoS_2 nanofilms and its application in improving hydrogen evolution reaction. Proc. Natl. Acad. Sci. USA 110, 19701–19706. https://doi.org/10.1073/pnas.1316792110.

Wang, L., Xu, Z., Wang, W., and Bai, X. (2014a). Atomic mechanism of dynamic electrochemical lithiation processes of MoS_2 nanosheets. J. Am. Chem. Soc. 136, 6693–6697. https://doi.org/10.1021/ja501686w.

Wang, N., Li, J., Hu, R., Zhang, Y., Su, H., and Gu, X. (2018). Enhanced catalytic performance and promotional effect of molybdenum sulfide cluster-derived catalysts for higher alcohols synthesis from syngas. Catal. Today 316, 177–184. https://doi.org/10.1016/j.cattod.2018.03.007.

Wang, X., Shen, X., Wang, Z., Yu, R., and Chen, L. (2014b). Atomic-scale clarification of structural transition of MoS_2 upon sodium intercalation. ACS Nano 8, 11394–11400.

Wang, Y., Carey, B.J., Zhang, W., Chrimes, A.F., Chen, L., Kalantar-zadeh, K., Ou, J.Z., and Daeneke, T. (2016). Intercalated 2D MoS_2 utilizing a simulated sun assisted process: reducing the HER overpotential. J. Phys. Chem. C 120, 2447–2455. https://doi.org/10.1021/acs.jpcc.5b10939.

Weber, T., Muijsers, J.C., van Wolput, J.H.M.C., Verhagen, C.P.J., and Niemantsverdriet, J.W. (1996). Basic reaction steps in the sulfidation of crystalline MoO_3 to MoS_2, as studied by X-ray photoelectron and infrared emission spectroscopy. J. Phys. Chem. A 100, 14144–14150.

Xia, B., Liu, P., Liu, Y., Gao, D., Xue, D., and Ding, J. (2018). Re doping induced 2H-1T phase transformation and ferromagnetism in MoS_2 nanosheets. Appl. Phys. Lett. 113, 013101. https://doi.org/10.1063/1.5027535.

Yang, M., Li, S., Wang, Y., Herron, J.A., Xu, Y., Allard, L.F., Lee, S., Huang, J., Mavrikakis, M., and Flytzani-Stephanopoulos, M. (2014). Catalytically active Au-O(OH)$_x$- species stabilized by alkali ions on zeolites and mesoporous oxides. Science 346, 1498–1501.

Yang, Y.Q., Dai, S.J., Yuan, Y.Z., Lin, R.C., Tang, D.L., and Zhang, H.B. (2000). The promoting effects of La_2O_3 and CeO_2 on K_2MoS_4/SiO_2 catalyst for methanethiol synthesis from syngas blending with H_2S. Appl. Catal. Gen. 192, 175–180.

Yu, M., Kosinov, N., van Haandel, L., Kooyman, P.J., and Hensen, E.J.M. (2020). Investigation of the active phase in K-promoted MoS_2 catalysts for methanethiol synthesis. ACS Catal. 10, 1838–1846. https://doi.org/10.1021/acscatal.9b03178.

Yu, Y., Nam, G.H., He, Q., Wu, X.J., Zhang, K., Yang, Z., Chen, J., Ma, Q., Zhao, M., Liu, Z., et al. (2018). High phase-purity 1T'-MoS_2 and 1T'-$MoSe_2$ layered crystals. Nat. Chem. 10, 638–643. https://doi.org/10.1038/s41557-018-0035-6.

Zak, A., Feldman, Y., Lyakhovitskaya, V., Leitus, G., Popovitz-Biro, R., Wachtel, E., Cohen, H., Reich, S., and Tenne, R. (2002). Alkali metal intercalated fullerene-like MS_2 (M =W, Mo) nanoparticles and their properties. J. Am. Chem. Soc. 124, 4747–4758.

Zhang, L., Karakas, G., and Ozkan, U.S. (1998). $NiMoS/γ -Al_2O_3$ catalysts: the nature and the aging behavior of active sites in HDN reactions. J. Catal. 178, 457–465.

Zhang, R., Tsai, I.L., Chapman, J., Khestanova, E., Waters, J., and Grigorieva, I.V. (2016). Superconductivity in potassium-doped metallic polymorphs of MoS_2. Nano Lett. 16, 629–636. https://doi.org/10.1021/acs.nanolett.5b04361.

Zhang, Z., Li, W., Yuen, M.F., Ng, T.-W., Tang, Y., Lee, C.-S., Chen, X., and Zhang, W. (2015). Hierarchical composite structure of few-layers MoS_2 nanosheets supported by vertical graphene on carbon cloth for high-performance hydrogen evolution reaction. Nano Energy 18, 196–204. https://doi.org/10.1016/j.nanoen.2015.10.014.

STAR★METHODS

KEY RESOURCES TABLE

REAGENT or RESOURCE	SOURCE	IDENTIFIER
Chemicals, peptides, and recombinant proteins		
K_2CO_3	Tianjin Chemical Reagent Co., Ltd.	CAS: 584-08-7
$(NH_4)_6Mo_7O_{24} \cdot 4H_2O$	Tianjin Chemical Reagent Co., Ltd.	CAS: 12054-85-2
$mSiO_2 \cdot nH_2O$	Qingdao Meigao Group Co., Ltd.	CAS: SG09

RESOURCE AVAILABILITY

Lead contact

Further information and requests for resources should be directed to and will be fulfilled by the lead contact, Yongming Luo (environcatalysis@kust.edu.cn).

Materials availability

Materials generated in this study will be made available on reasonable request, but we may require a payment or a completed Materials Transfer Agreement if there is potential for commercial application.

Data and code availability

- Data reported in this paper will be shared by the lead contact upon reasonable request.

- The present research did not use any new codes.

- Any additional information required to reanalyze the data reported in this paper is available from the lead contact upon reasonable request.

METHOD DETAILS

Catalyst preparations

Microspherical silica supported K_2MoO_4 materials (K-Mo/MS) were firstly prepared via incipient-wetness impregnation method. Typically, the appropriate volume of potassium carbonate (K_2CO_3) and ammonium molybdate (($NH_4)_6Mo_7O_{24} \cdot 4H_2O$) was dissolved into deionized water (the molar ratio of K/Mo is 2 and the loading of Mo species calculated as MoO_3 is 20 wt.%), and then microspherical silica ($mSiO_2 \cdot nH_2O$, Qingdao Meigao Group Co., Ltd.) was added and mixed completely. The impregnated solids were standing at room temperature for 12 h and dried at 120°C for 6 h, and then calcined in air at 550°C for 6 h with a ramp rate of 2 °C/min.

0.4 g of the oxidized catalysts with the mesh of 40–60 was sulphided at different annealing temperature (280, 300, 320, 360, 400°C, respectively) for 2 h with a heating rate of 2 °C/min in the atmosphere of 10 vol.% H_2S/H_2 mixtures (20 mL/min). After vulcanization, supported K-intercalated 1T′-MoS_2 and K-decorated 2H-MoS_2 materials were controllably synthesized, and then used for the characterization and activity measurements.

Unsupported K_2MoO_4 material was prepared via the mechanical grinding method. Typically, a certain amount of potassium carbonate and ammonium molybdate with the K/Mo molar ratio of 2 was added into the mortar and grinded completely with pestle for 40 min. Then, the grinded samples were calcined in the muffle at 700°C for 2 h (2 °C/min).

The prepared K_2MoO_4 oxides with the mesh of 40–60 (0.4 g) was sulphided at different annealing temperature (20, 80, 160, 180, 200, 220, 240, 280, 320, 360, 400°C) in the same atmosphere for 2 h. The sulphided samples were ready for the characterizations.

Characterizations of the catalysts

Raman spectra of the samples were recorded by a Renishaw Invia Raman imaging microscope with a 532 nm laser excitation. X-ray photoelectron spectroscopy (XPS) was recorded on a PHI 5000 Versa Probe II with an aluminum anode (Al Kα = 1486.6 eV). All the binding enegies of all the spectra were calibrated by C 1 s peak at 484.8 eV. Casa XPS software was used to deconvolute the measured signals, employing a Gaussian-Lorentzian curves and a Shirley background correction. The amounts of K-intercalated MoS_2 and K-decorated MoS_2 were calculated by the peak area ratios of Mo/Si normalized by the corresponding atomic sensitivity factors. High-angle annular dark-field scanning transmission electron microscopy (HAADF-STEM) and EDX mapping measurements were carried out on a FEI Titan Themis 200 electron microscope and operated at an acceleration voltage of 200 kV. The sulfided samples were finely ground in mortar in a nitrogen-filled glovebox and immersed in ethanol. Then, a few droplets were dropped on a copper grid deposited with a carbon film, and then the Cu grid was transferred into one sealed container for measurements. The EDX line-scan results were obtained by processing the data of EDX mappings using GMS 3 software in the company of GATAN. X-ray diffraction (XRD) patterns were collected on a Rigaku D/Max-1200 diffractometer with Cu Kα radiation (40 kV, 30 mA). Temperature programmed reduction (TPR) of H_2 experiments were carried out with a thermal conductivity detector (TCD). H_2-TPR measurements of the catalysts (50 mg) were performed in a flow of 10 vol. % H_2/Ar (30 mL/min) from RT to 800°C with a ramping rate of 10 °C/min. Temperature programmed desorption (TPD) of CO, H_2S, H_2 experiments were also performed by TCD. For a typical procedure, the sulphided catalysts were first pretreated at 280°C for 30 min in the inert atmosphere, then the temperature was decreasing to 30°C, 10% CO/He, 10% H_2/Ar, and 10% H_2S/He were introduced into the reaction system, and the samples were adsorbed respectively in the atomsphere for 60 min to arrive the saturated adsorption capacity. After purging in the corresponding inert atmosphere (He, Ar, He) until the physically adsorbed species was removed, all the experiments of CO-TPD, H_2-TPD, and H_2S-TPD were carried out by elevating temperature up from 30°C to 800°C with a heating rate of 10 °C/min using He, Ar and He as carrier gas, respectively. Moreover, to verify the role of surface active sulfur on the adsorption property of H_2, 10% CO/40 %H_2/Ar was used to pretreat the sulphided sample at 280°C for 30 min in order to remove the surface active sulfur species.

Catalytic performance evaluation

The performance for the synthesis of CH_3SH from CO/H_2/H_2S as one typical thermocatalytic reaction was evaluated using a fixed-bed microreactor under the atmosphere pressure, where catalysts were loaded into a quartz tube with an inner diameter of 6 mm. Notably, the gas-tightness of reaction systems should be checked in advance due to the high concentration of toxic and harmful gases. Before measurements, 0.4 g of the catalyst was *in-situ* pre-sulphided in 10 vol. % H_2S/H_2 (20 mL/min) at 280, 300, 320, 360, 400°C, respectively, for 2 h as performed in the Section of catalyst preparation. Subsequently, the catalyst bed was purged with high purity nitrogen for 30 min, and then the feed gas containing a composition of 10% CO, 40% H_2 and 50% H_2S with the flow rate of 40 mL/min was introduced. The activity tests were conducted at 280°C for 5 h under kinetic regime with CO conversion below 20% after the relative steady state was achieved. The mass transport related problems were excluded by using the Weisz criterion method. Quantitative analysis of reactant (CO) and products (CH_3SH) was accomplished with a FULI GC 9790 gas chromatograph with two flame photometric detector (FPD), a flame ionization detector (FID) and two thermal conductivity detector (TCD). The reaction rate of CO ($R_{CO\ reaction}$) and the formation rate of CH_3SH ($R_{CH3SH\ formation}$) were calculated according to Equations 1 and 2, respectively.

$$R_{CO\ reaction} = \frac{F_{CO}}{n_{Mo}} \cdot X_{CO} \qquad \text{(Equation 1)}$$

$$R_{CH_3\ SH\ formation} = \frac{F_{CH_3\ SH}}{n_{Mo}} \qquad \text{(Equation 2)}$$

where F_{CO}, and F_{CH3SH} is the molar flow of CO, and the formation amount of CH_3SH ($mol_{CO}s^{-1}$ and $mol_{CH3SH}s^{-1}$), respectively; X_{CO} is the conversion of CO; n_{Mo} is the molar fraction of Mo (mol_{Mo}) based the actual loading of MoS_2.

QUANTIFICATION AND STATISTICAL ANALYSIS

Our study doesn't include quantification and statistical analysis.